NEAR-SURFACE STRUCTURE OF THE SAN ANDREAS FAULT, SAN FRANCISCO PENINSULA SEGMENT

A thesis submitted to the faculty of
San Francisco State University
in partial fulfillment of
the requirements for
the degree

Master of Science
In
Geosciences

by

Carla Marie Rosa

San Francisco, California

December 2013

CERTIFICATION OF APPROVAL

I certify that I have read *Near-Surface Structure of the San Andreas Fault, San Francisco Peninsula Segment* by Carla Marie Rosa, and that in my opinion this work meets the criteria for approving a thesis submitted in partial fulfillment of the requests for the degree: Master of Science in Geosciences at San Francisco State University.

Karen Grove
Professor, Department of Earth & Climate Sciences

Leonard Sklar
Associate Professor, Department of Earth & Climate Sciences

Rufus Catchings
Research Geophysicist, U.S. Geological Survey

Michael Rymer
Scientist Emeritus, U.S. Geological Survey

NEAR-SURFACE STRUCTURE OF THE SAN ANDREAS FAULT, SAN FRANCISCO PENINSULA SEGMENT

Carla Marie Rosa
San Francisco, California
2013

High-resolution seismic images were developed using both seismic refraction and reflection profiling from coincident P- and S-wave seismic data acquired near Woodside, California, in June 2012. A 60-m-long seismic profile was approximately centered on the 1906 surface rupture of the Peninsula segment of the San Andreas Fault (SAF). The data were acquired and processed with methods previously used by the U.S. Geological Survey in other successful studies. The seismic images suggest the presence of possibly three near-surface fault traces within about 25 m of the main 1906 surface rupture. A P-wave, high-velocity zone relates to a significant fault trace observed southwest of the main 1906 fault trace that does not appear to break the surface. This trace may be associated with long-term movement prior to the main 1906 break, and the fault traces observed may merge at depth. The reflection image displays strong, near-vertical diffractions, particularly beneath the P-wave, high-velocity zone, consistent with fault traces inferred from the seismic images. A borehole augered into this P-wave, high-velocity zone revealed bright blue clay, possibly originating from weathered serpentinite. Because this study found evidence for multiple fault traces in the SAF zone, it is possible that slip histories for the Peninsula segment of the SAF may have been miscalculated. Further work in geophysics and especially paleoseismology is needed to better constrain the geometry and slip history of the Peninsula segment of the SAF.

I certify that the Abstract is a correct representation of the content of this thesis.

Chair, Thesis Committee — 12/18/13 Date

ACKNOWLEDGMENTS

I thank my advisor Dr. Karen Grove for encouraging me to further my education at San Francisco State University, which allowed me to produce this research. My deepest thanks to my committee members Dr. Rufus Catchings, with whom I spent many months learning these geophysical methods in depth, and to Michael Rymer for helping me find the perfect research area. Thank you also to my committee member Dr. Leonard Sklar for his insight and advice throughout this process. I am very grateful to everyone who assisted me with data acquisition: Rufus Catchings, Mark Goldman, Coyn Criley, Alex Barker, Elizabeth Rose, Alex Ferguson, Will Hassett, Neil Fenning, Aaron Perkins, and Leah Campbell. Thank you to Robert Sickler and Jim Lienkaemper for helping me acquire the GPS data. I am eternally grateful to the Earthquake Science Center of the U.S. Geological Survey in Menlo Park, California and Rufus Catchings, who very generously provided funding for this research. Carol Prentice, Judy Zachariasen, and Robert Sickler provided paleoseismic data, which was very important for this study. I also thank the San Francisco Public Utilities Commission for allowing me to conduct research on their watershed land. Finally, many thanks to my family and friends for their moral support, especially my mother for her unconditional love and comfort and Alex Barker for his patience and total encouragement.

TABLE OF CONTENTS

TABLE OF CONTENTS

LIST OF TABLES

LIST OF FIGURES

INTRODUCTION

The San Andreas Fault (SAF) is a continental transform fault that extends through much of California and spans a length of approximately 1,300 km (Figure 1; Wallace, 1990). The San Andreas Fault system (SAFS) formed when the Pacific plate first encountered the North American plate to create a transform boundary about 27 Ma (Atwater, 1989). This boundary is complex, with numerous curved strands that create areas of transpressional and transtensional deformation (Argus and Gordon, 2001). Cumulative right-lateral displacement along the SAF has resulted in at least 300 km of offset and, as a result, the SAF juxtaposes distinctively different basement rock types. For example, in central and northern California, there are oceanic Jurassic–Cretaceous Franciscan Complex rocks to the northeast of the SAF and Mesozoic continental plutonic and older metamorphic rocks of the Salinian terrane to the southwest (Figure 2; Irwin, 1990). Locally, however, there are several exceptions to this generalization (see Rymer et al., 2006, Figure 4). My study area on the San Francisco peninsula is one of these exceptions, where the Pilarcitos Fault (west of the SAF) is the bedrock boundary, and Franciscan Complex rocks are exposed on both sides of the SAF (Figure 2; Parsons and Zoback, 1997).

In the San Francisco Bay Area (SFBA), the SAFS is an approximately 80-km-wide zone of mostly right-lateral, strike-slip faults that mark the boundary between the Pacific plate and the Sierra Nevada–Great Valley microplate (Figure 1; Wallace, 1990; Argus and

Gordon, 2001). This plate boundary also includes thrust and reverse faults and folds, which accommodate some of the transform and all of the contractional motion that is responsible for uplift of the California Coast Ranges (Argus and Gordon, 2001). In the SFBA, the fault system is composed of four principal fault strands: the San Gregorio Fault, the Peninsula segment of the SAF, the Rodgers Creek-Hayward Fault, and the Green Valley-Concord-Calaveras Fault (Figure 1; Savage et al., 1999). These principal faults and many other smaller faults accommodate about 40 mm/yr of plate boundary motion through right-lateral shear between the Pacific and Sierra Nevada-Great Valley plates (Figure 1; Parsons and Zoback, 1997). Within the SAFS, the San Gregorio Fault is a major onshore and offshore structure that is located west of the SAF and accommodates approximately 6 mm/yr of slip, which is transferred to the SAF south of Point Reyes (Figure 1; Wesnousky 1986; Argus and Gordon, 2001; d'Alessio et al., 2005). On the Peninsula segment of the SAF, estimates for the long-term slip rate range from 14.5 to 23 mm/yr (Kelson et al., 1996; Savage et al., 1999; WGCEP, 2008). Collectively, other faults of the East Bay region accommodate the remaining motion, most notably through movement on the Rodgers Creek (9–11.5 mm/yr), Hayward (9 mm/yr), Green Valley (10 mm/yr), and Calaveras (4–8 mm/yr) faults (Figure 1; Kelson et al., 1996; Savage et al., 1999; WGCEP, 2008). Due to the active plate-boundary motion occurring in the SFBA, it is important to investigate for the existence of faults in addition to those mapped in trench exposures, particularly along relatively poorly understood faults such as the Peninsula segment of the SAF, which is the focus of this study.

The SAF that ruptured in 1906 is divided into four segments (the shortest section capable of repeatedly rupturing) with differing characteristics: average strike, recurrence interval, slip rate, and age of the penultimate earthquake (WGCEP, 2003; 2008). These segments are, from south to north, the Santa Cruz Mountains, Peninsula, North Coast, and Offshore segments (Figure 1; WGCEP, 2003; 2008). These segments reflect the idea that some earthquakes on the northern SAF result from rupture of a single segment of the fault, whereas some earthquakes result from rupture of multiple segments, as in 1906.

The Peninsula segment of the SAF, which includes the area of this study, extends southeast about 85 km, from offshore of the Golden Gate, near the epicenter of the 1906 earthquake, to near Los Gatos at the north end of the Loma Prieta aftershock zone (Figure 1; Hall et al., 2001; WGCEP, 2003).

In this thesis, I present the survey acquisition parameters, data and interpretations, and discuss the significance of a 60-m-long, high-resolution seismic-imaging survey across the 1906 SAF surface rupture zone. The survey was conducted near the Filoli Center in Woodside, California, approximately 1.2 km southeast of Upper Crystal Springs Reservoir, on the Peninsula segment of the SAF (Figures 1, 3, and 4). Further work involving a hand-augered borehole was also done along the seismic profile to better understand the subsurface material.

The seismic images show details of the subsurface structure, which can help to understand the local structural setting and history of the Peninsula segment of the SAF. If subsidiary faults are present, the hazards associated with surface rupture of the SAF should be reassessed because movement on a multiple-strand fault can produce locally varying amounts of right-lateral slip. The seismic images can aid paleoseismological studies in identifying additional rupture zones so that average recurrence intervals and slip rates can be more accurately calculated, and thus, seismic hazards models for the Peninsula segment of the SAF can be improved.

REGIONAL TECTONIC SETTING

The SAF accommodates more than half of the dextral slip in the SFBA, and three of the four historical $M \geq 6.7$ earthquakes (1838, 1906, and 1989) have occurred on or near the SAF (Figure 1; WGCEP, 2003). By 2031, there is a 62% probability of at least one $M \geq 6.7$ earthquake occurring in the SFBA, with a 21% probability of one happening on the SAF (WGCEP, 2003). For larger magnitude earthquakes, $M \geq 7.5$, the probability is much lower at 10% by 2031, although only the SAF and the San Gregorio Fault have the capability of generating a $M \geq 7.5$ earthquake owing to their great lengths (WGCEP, 2003). Although it has been concluded that the probability of a destructive earthquake occurring in the SFBA by 2031 is high, this only partially describes the seismic hazard in the SFBA. Most of the damage caused by an earthquake is from strong ground shaking, which depends not only on the size of the earthquake, but also on hypocentral distance from the causative fault, local lithological and stratigraphic properties, the direction of rupture, and the duration of shaking (WGCEP, 2003).

Earthquake damage in the SFBA over the past few centuries has been variable, with little or no damage during periods of relative seismic calm, and significant damage during intervals with more intense seismic activity (WGCEP, 2003). Median ground motions and intensity levels occurring during earthquakes can be estimated using the modified Mercalli intensity scale (MMI), designed by Wood and Neumann (1931) (Table 2). This scale quantifies the effects of an earthquake on the Earth's surface, people, engineered structures, and natural objects on a scale from I (not felt) to XII (total destruction) (Table 2). Over the past 170 years, the SFBA has experienced an earthquake with MMI VII or greater intensity on an average of every 30 to 50 years (WGCEP, 2003). On the Peninsula segment of the SAF, with a probable recurrence interval of 229 years (WGCEP, 2003), a M 7.2 event (similar to 1838) would produce damaging ground motions (MMI-VIII) along the Peninsula and around much of the Bay margin (WGCEP, 2003). An event on the Peninsula could produce almost 900 road closures, mainly in San Francisco and San Mateo counties (WGCEP, 2003). Of the four segments of the northern SAF, the Peninsula segment is the segment most likely to rupture in a M $\geq$6.7 event (WGCEP, 2003). Historically, the Peninsula segment of the SAF last ruptured as part of the full, four-segment rupture observed during the 1906 earthquake. The Peninsula segment is also thought to have ruptured during the smaller 1838 event (estimated at M 6.8-7.4), although there is no clear evidence placing this event on the SAF (WGCEP, 2003). Inconsistencies between earthquake records at several different paleoseismic sites on the Peninsula segment of the SAF bring to light possible errors in current seismic hazard models that rely on these results and the need to better understand the structural setting and history of the fault. Because of these factors, this study aims to gather more information on the Peninsula segment of the SAF, which remains poorly understood. Thus, it is critically important to determine the exact location of the main trace and potential auxiliary traces of the SAF for further paleoseismic research to build a more accurate event history and properly determine the regional seismic hazard. My study, which involves high-resolution seismic data along the Peninsula segment of the SAF, helps to clarify the precise locations of near-surface fault traces.

BACKGROUND

Geologic Setting

In central and northern California, the SAF marks the boundary between Mesozoic granitic basement rocks of the Salinian terrane to the southwest and Jurassic-Cretaceous Franciscan Complex rocks to the northeast (Figure 2; Irwin, 1990; Pampeyan, 1994). However, south of San Francisco, the Pilarcitos Fault, an ancestral plate-boundary fault, forms the basement boundary. East of the Pilarcitos Fault, the SAF passes through Franciscan Complex rocks, such that Franciscan rocks are located on both sides of the fault (Figure 2; Pampeyan, 1994; Brabb et al., 2000). The Pilarcitos Fault is important to this study because it results in having Franciscan Complex rocks on both sides of the SAF, and thus imaging, especially conventional seismic-reflection imaging, is much more difficult and/or rendered useless.

The Franciscan Complex consists of Jurassic–Cretaceous-aged rocks that were formed through convergent plate interaction when the Pacific plate was being subducted beneath the North American continental margin (Page, 1981; Pampeyan, 1994; Brabb et al., 2000). Franciscan Complex rocks are weakly to strongly metamorphosed and locally consist of sandstone, greenstone, serpentinite, chert, schist, and limestone in a sheared mudstone matrix mélange (Figure 2; Pampeyan, 1994; Brabb et al., 2000). These rock deposits are found at the study area (Brabb et al., 2000), creating complex strata that dramatically affect what can be seismically imaged with conventional reflection techniques.

West of the Pilarcitos Fault, Mesozoic plutonic rocks of the Salinian terrane are pervasively fractured rocks that are part of larger batholithic complexes that formed in southern California. The SAF has displaced the Salinian terrane northward more than 300 km (Figure 2; Irwin, 1990).

Other ancient rocks in the region include upper Mesozoic sedimentary rocks of the Great Valley sequence (Late Jurassic and Cretaceous) that are composed mostly of highly folded marine sandstone, shale, and conglomerate formed primarily by turbidity flows (Figure 2; Page, 1981; Brabb et al., 2000). These rocks are locally overlain by younger deposits, which include Paleocene turbidite sequences of sandstones, shales, and conglomerates that are highly folded (Page, 1981; Pampeyan, 1994). Mafic volcanic rocks of Oligocene–Miocene age are present east of the study area (Figure 2; Pampeyan, 1994). Neogene sedimentary rocks in the region include the Purisima Formation that is composed of shallow-marine pebble-conglomerate to fine-grained sandstone, and the Merced Formation, composed of coastal-marine sand and mud (Pampeyan, 1994).

Quaternary deposits near my study area include landslide deposits, ravine fill, and debris-flow material along with stream deposits, alluvium, and local lake deposits (Page, 1981; Pampeyan, 1994). The sediments that lie beneath and adjacent to the water of the San Francisco Bay are composed mainly of silt and clay; this bay mud is water saturated and susceptible to liquefaction during an earthquake (Figure 2; Page, 1981; Pampayen, 1994). Sedimentary deposits in the study site are Pliocene to Pleistocene in age and include the non-marine Santa Clara Formation, which consists of conglomerate, sandstone, and mudstone (Brabb et al., 2000). Pleistocene coarse grained alluvial fan and fluvial terrace deposits, containing poorly consolidated gravel, sand, and silt can also be found at the study site (Brabb et al., 2000).

The site chosen for this study is located between the Filoli Center and Upper Crystal Springs Reservoir, in the San Francisco Public Utilities Commission (SFPUC) Peninsula Watershed (Figure 4). This site was selected due to its proximity to previous and ongoing paleoseismic investigations (Figure 3). Here, the SAF trends along the eastern edge of the Santa Cruz Mountains, marking the western edge of the San Andreas linear fault valley that is flooded by the Crystal Springs Reservoir (Figure 4). The 1906 surface trace of the SAF here displayed west-side-up vertical displacement, which, through multiple earthquake cycles, has resulted in a 5–10-m-high northeast-facing scarp along the foot of the mountains (Zachariasen et al., 2011).

In the study area, Spring Creek drains an area of about 3 km^2 on the northeast margin of the northern Santa Cruz Mountains, where it has deposited sediments and constructed an alluvial fan across the active fault zone during the Holocene (Figure 4). Immediately to the southeast of the site, Spring Creek breaches the scarp near the head of an alluvial fan (Figure 4). Trenching at the site of the seismic line has exposed fluvial channel and overbank deposits overlying a dark grey clayey deposit containing weathered pebble-sized clasts, as well as multiple generations of faults with evidence for movement during past events (Table 1; Zachariasen et al., 2011).

Earthquake History

The earthquake record for the Peninsula segment of the SAF is important because this segment poses a significant hazard for the SFBA, yet little is known about the occurrence of earthquakes prior to the M 7.9 April 18, 1906 event. Paleoseismic investigations in the area have attempted to produce a more detailed paleoseismic history. This history is not well constrained, as described in subsequent sections and summarized in Table 1.

1906 Earthquake

According to Hall et al. (2001), the Peninsula segment of the SAF has been active throughout the Holocene, with surface ruptures along multiple fault traces. The most recent surface rupture occurred during the April 18, 1906 M 7.9 San Francisco earthquake (Lawson, 1908). In this event, the surface rupture extended about 470 km, from near San Juan Bautista in the south to the Mendocino triple junction in the north (Figure 1A; Prentice, 1999), and included all four segments: the Offshore, North Coast, Peninsula, and Santa Cruz Mountains segments (Figure 1B; WGCEP, 2003; 2008). About 4.9 to 5.5 m of offset was observed near Point Reyes (Figure 1; Niemi and Hall, 1992) on the North Coast segment of the SAF; however, on the Peninsula segment, Hall (1984) suggested there was only about 3 m of offset based on paleoseismic evidence along the fault near Crystal Springs Reservoir in San Mateo County, where 90% of the motion was distributed across a 30-m-wide zone (Figure 1). South of Woodside in Portola Valley (Figure 1B), offset from the 1906 event decreased significantly and was probably about 1.2 m (Lawson, 1908; Hall et al., 2001).

Penultimate Earthquake

Prior to the 1906 event, the paleoearthquake record for the Peninsula segment of the SAF has yielded inconsistencies about the age and extent of the penultimate (second to last) event. Toppozada and Borchardt (1998) and Bakun (1999) both modeled intensity data in the region, which indicated that the historical June 1838 earthquake was located somewhere on the peninsula (Figure 1). Based on newspaper articles and other evidence of damage and shaking in Monterey and San Francisco following the 1838 event, Toppozada and Borchardt (1998) suggested the 1838 event ruptured an ~140-km-long segment of the SAF rather than the shorter 60-km-long rupture length previously assumed. The longer rupture length implies the event had a magnitude on the order of M ~7.5. Bakun (1999), however, estimated a M 6.8 for the 1838 event, based on MMI ratings at various locations around the Bay Area, and he further determined that the epicenter of the June 1838 earthquake was near Woodside (Figure 3). Current earthquake hazard assessments for the Bay Area assume that the 1838 event occurred on the Peninsula segment of the SAF, although direct paleoseismic evidence remains absent.

Past Paleoseismic Studies

Although there have been numerous paleoseismic studies on the SAF, minimal work has been done on the Peninsula segment, of which there are several conflicting results with respect to its paleoearthquake record (Table 1; Figure 3; Hall et al., 1999; Baldwin et al., 2006; Prentice and Moreno, 2007; Baldwin and Prentice, 2008; Prentice et al., 2008; Zachariasen et al., 2011).

In a study of long-term slip, Hall et al. (1999) excavated many fault-perpendicular and fault-parallel trenches at the Filoli site, where late Holocene alluvial fan materials were deposited over the fault (Figure 3). They calculated an average late Holocene slip rate of 17 ± 4 mm/yr for the Peninsula segment of the SAF (Table 1). This calculation was based on 30 ± 2 m offset of the thalweg of a well-defined stream channel deposit that was dated at 2070 ± 120 years B.P. (Hall et al., 1999). Although efforts to develop a longer event record were somewhat unsuccessful due to the presence of coarse-grained and discontinuous deposits, Hall et al. (1999) inferred evidence for two late Holocene earthquakes from channel deposits that were projected toward the fault from both sides of fault-parallel trench walls that were cut back to within a few meters of the fault (Hall et al., 1999). The youngest of these nested channels, dated at 150 ± 150 years B.P., was offset about 2.5 ± 0.5 m, which they determined was the result of the 1906 earthquake because of its similarity to slip measured nearby (Hall et al., 1999). The older, and stratigraphically lower, channel deposit, dated at 330 ± 200 years B.P., is offset 4.1 ± 0.5 m, which was attributed to both the penultimate earthquake with 1.6 ± 0.7 m of dextral offset, and the 1906 event with about 2.5 m of slip (Hall et al., 1999). Because the penultimate earthquake has an estimated offset smaller than 1906, they suggested that this earthquake likely ruptured a shorter section of the fault than in 1906, possibly only the Peninsula segment of the SAF with a likely magnitude of about M 7.0–7.4 (Hall et al., 1999). Based on the poorly constrained age of the inferred older event and taking into account their assumptions of the likely rupture length, Hall et al. (1999) proposed that the 1838 earthquake, which occurred somewhere on the Peninsula, was a probable fit for the event (Table 1; Hall et al., 1999). Although this hypothesis was speculative, the 1838 event has been generally considered to have occurred on the Peninsula segment of the SAF (Zachariasen et al., 2011). Recently, however, Zachariasen et al. (2010) reinterpreted the Hall et al. (1999) data and suggested the older channel was offset by only the 1906 event, and that, thus, there is no direct evidence for a pre-1906 event (in the span of the past few hundred years) at the site.

In a more recent paleoseismic investigation along the Peninsula segment, about 10 km northwest of my study area at the northern end of Lower Crystal Springs Reservoir, Prentice and Moreno (2007) excavated a trench where they identified the 1906 rupture and one previous event (Table 1; Figure 3). Although the age of the older event was not reported, sediments that bracket the event lack European pollen, suggesting the event preceded the 1820 start of European settlement (Prentice and Moreno, 2007). Further age constraints suggested the older event occurred between AD 890–1260 and a second trench located at Lower Crystal Springs Reservoir only showed evidence for the 1906 earthquake, but no event predated the 1906 event within a 3-m-deep exposure (Table 1; Figure 3; Prentice et al., 2008). Prentice et al. (2008) offered several reasons to explain these conflicting observations, including: (1) high sedimentation rates during the late 19^{th} and 20^{th} centuries, masking the 1838 event horizon; (2) the penultimate earthquake may have occurred prior to the 19^{th} century; and (3) a depositional gap between the faulted and unfaulted sediments, implying that multiple earthquakes may be represented in the event horizon.

In a trench at Portola Valley Town Center, about 16 km southeast of my site, Baldwin et al. (2006) and Baldwin and Prentice (2008) interpreted evidence for the presence of at least three, and possibly four, pre-1906 events in about 1,000 years (Table 1; Figure 3). Evidence for these events includes dipping marsh and fluvial deposits, potential fissure fills, and colluvial wedge units (Baldwin et al., 2006; Baldwin and Prentice, 2008). Based on radiocarbon dating, events are interpreted as occurring at: (1) AD 1,030 to 1,490, (2) AD 1,260 to 1,490, and (3) AD 1906 (Baldwin and Prentice, 2008). The data allow for a possible alternative interpretation of the second event as two events (AD 1,260 to 1,490 and AD 1,410 to 1,640) (Baldwin and Prentice, 2008). Although some of these ages for events are consistent with results at other sites, evidence for an 1838 event was not found.

At my study site 1.2 km southeast of Crystal Springs Reservoir (Figure 3), Zachariasen et al. (2011) excavated two cross-fault trenches that exposed fluvial deposits (~1,000 years old) overlying an older (~3,100 years old) clay-rich unit. Zachariasen et al. (2011) found evidence to suggest that only two events occurred during the past 1,000 years: one in

1906, and the other 600–1,000 years ago (Table 1). They found no direct evidence that the 1838 earthquake involved surface rupture on the 1906 trace of the SAF (Table 1). This record of two earthquakes in 1,000 years is similar to the paleoseismic record of Prentice et al. (2008) at Crystal Springs Reservoir to the northwest (Figure 3). Conversely, evidence of three to four events in 1,000 years was observed at the Portola Valley Town Center site to the southeast (Figure 3).

WGCEP (2003, 2008) relied on historical and paleoseismic observations to create rupture models that included scenarios involving rupture of the full fault length (as in 1906) or rupture of one, two, or three segments. Based on similar ages for several events observed on the North Coast and Santa Cruz Mountains segments that are inferred to be the same event, the WGCEP (2003; 2008) favored rupture models where the entire northern SAF ruptures. However, the timing of some of these past events differs among segments, suggesting that some earthquakes on the SAF could involve smaller ruptures (Zachariasen et al., 2011). Although many paleoseismic investigations of the Peninsula segment have been done, their conflicting results bring into question the validity of earthquake records at various sites and the seismic hazard models that these are based on. Further paleoseismic research on the Peninsula segment, including investigations on potential auxiliary traces, is needed to accurately determine its event history and refine existing rupture models for the SAF. As summarized below, my seismic images suggest that there may be more than one near-surface fault trace within 30 m of the main 1906 surface rupture. This allows that earlier events may have occurred on the main 1906 surface trace or one of the other newly inferred fault traces. High-resolution seismic images of the area could be useful in identifying near-surface fault traces that may clear up the discrepancies between the paleoseismic studies that could then lead to a more accurate determination of slip rates and recurrence intervals.

GEOPHYSICAL METHODS

To measure seismic velocities and better understand the near-surface structure of the Peninsula segment of the SAF, both high-resolution seismic refraction tomography and reflection methods were used to conduct a more thorough seismic survey of the area. This combined study provides multiple images of fault structure based on independent measures. These methods were developed by the High-Resolution Seismic Imaging group of the U.S. Geological Survey (USGS) in Menlo Park, California (see Catchings et al., 2013). Near-surface fault zone imaging is important because surface rupture, strong ground motions, and paleoseismic investigations occur in the near surface and geophysical methods can locate previously unknown faults that are not apparent at the surface due to burial by young sedimentary deposits. The combined methods are essential in characterizing the SAF structure in my study area, where the main 1906 surface-rupture zone is located in an area of geologic complexity. Groundwater saturation, compaction, and fracturing create geologic complexity in the uppermost few tens of meters that make near-surface seismic reflection imaging of fault zones difficult

(Catchings et al., *in review*), so refraction methods are employed as well. These images are used to interpret the subsurface structure based on interfaces between materials with varying physical properties that reflect or refract the seismic waves.

General Seismic Principles

The main objective of seismic surveying is to image and understand the geometry of subsurface units. Surface-based seismic surveys measure the time it takes for seismic energy originating at the surface to travel through the subsurface to various interfaces and back to the surface, where the energy is sensed by geophones. A seismic source causes local deformation in elastic media, such as rocks, that propagates away from the source as seismic waves (Figure 5; for example, see Burger et al., 2006). In the subsurface, seismic energy travels in waves that spread out as hemispherical wavefronts (Figure 5). Raypaths, which are vectors perpendicular to the wavefront, are a mathematical representation of the paths of the energy arriving at the geophones (Figure 5). The types of waves that are most used for exploration in seismic studies are body waves, which travel through the Earth. Body waves include primary (P) and shear (S) waves. In contrast to body waves, surface waves (Love and Rayleigh waves) add noise to the body-wave seismic signal, and processing steps are needed to remove this noise from the seismic record.

The behavior of seismic waves in the subsurface is modeled as an interaction of body waves with planar interfaces. In the subsurface, seismic energy is refracted (i.e., bent) and/or reflected back to the surface when the ray reaches interfaces between materials with different acoustical impedances (Figure 6). Acoustical impedance represents differences in density, seismic velocity, or both and contrasts typically occur at boundaries between geologic layers (for example, see Steeples and Miller, 1990). Variations in seismic velocities can be present between different rock types, or between similar rock types that vary in water saturation. At an interface in the subsurface, some of the seismic energy is refracted (i.e., transmitted) to the deeper medium, while some energy is reflected back into the upper medium. Where velocity increases with depth, seismic waves are refracted back to the surface. Refracted waves also propagate along the boundary with the lower layer's higher velocity, returning energy to the surface faster than any other wave (Figure 6; for example, see Burger et al., 2006). Some seismic waves are reflected back to the surface when they reach an interface between materials with distinctive acoustical impedance contrasts (Figure 6).

Propagation of Seismic Waves in Fault Zones

Seismic P-wave velocity (Vp) can be defined by:

$$\mathrm{Vp} = \sqrt{K + \frac{4}{3\mu} / \rho} \qquad (1)$$

where K is the bulk modulus, a measure of the incompressibility of subsurface materials,
μ is the shear modulus, a measure of the material rigidity, and
ρ is the density of a homogeneous isotropic media (for example, see Dobrin and Savit, 1988; Sleep and Fujita, 1997; Catchings et al., *in review*).

Therefore, P-waves will propagate through most materials, including fluids. S-wave velocity (Vs), however, is defined only in terms of the shear modulus and the subsurface material's density (for example, see Dobrin and Savit, 1988; Sleep and Fujita, 1997; Catchings et al., *in review*):

$$Vs = \sqrt{\mu/\rho} \tag{2}$$

S-waves will not propagate in materials that lack rigidity, such as fluids, and Vs will decrease in materials with relatively low-rigidity (Nur and Simmons, 1969). Near-surface P- and S-wave propagation differ due to the extent of shearing and rock damage, variations in groundwater saturation, and compaction (Catchings et al., *in review*).

Shearing can damage host rocks up to hundreds of meters away from the epicenter of an earthquake (Flinn, 1977; Wallace and Morris, 1986; Wilson et al., 2003; Sibson, 2003; Chester et al., 2005), significantly reducing the bulk and shear moduli in the damaged rock (Chester and Logan, 1986; Gupta and Bergstrom, 1998), especially if there is a high clay content (Wu, 1978; Han et al., 1986). Because of this, fault zones are typically lower in velocity than the adjacent host rocks (Mayer-Rosa, 1973; Healy and Peake, 1975; Aki and Lee, 1976; Wang et al., 1978; Spudich and Angstman, 1980; Mooney and Luetgert, 1982; Thurber, 1983; Mooney and Ginzburg, 1986; Li and Leary, 1990; Catchings et al., 2002; 2009; 2013; *in review*).

Groundwater saturation highly affects Vp in the near surface because saturated materials usually have higher Vp than similar unsaturated and partially saturated materials because of the higher incompressibility (K) of the saturated materials. Vs is not as affected by groundwater because S-waves do not have a bulk modulus term and are instead affected by the rigidity (μ) and density, and density is the only term that is significantly changed with increasing groundwater saturation.

Faulting creates elongated cracks and fractures in rock, which reduce both the incompressibility and rigidity of rocks, causing low Vp and Vs. Compaction can cause cracks to close, thereby increasing the incompressibility and rigidity, and causing higher Vp and Vs values (Nur and Simmons, 1969). Therefore, seismic velocities that are decreased by faulting can be opposed by high levels of groundwater saturation and compaction in the near-surface, causing seismic velocities in the near-surface to appear more wide-ranging than at greater depths (Catchings et al., *in review*).

Tomographic Imaging of Fault Zones in the Vadose Zone

Vp is highly variable in the vadose zone (above the groundwater table) due to variations in subsurface structure and groundwater saturation, so tomographic imaging of fault zones using P-waves can be more complex in the vadose zone than at greater depths (Catchings et al., *in review*). Vp decreases with increasing saturation levels up to 90% and increases sharply thereafter (Nur, 1982). Increasing density due to increased saturation causes the initial drop in Vp, but above 90% saturation, Vp increases because of the markedly increased incompressibility of the saturated materials (King, 1966; Domenico, 1974; 1977; Nur and Simmons, 1969; Nur, 1982; Zhu et al., 2000; Wang, 2001). Because faults often act as barriers to groundwater flow (Tolman 1937; Dutcher and Garrett, 1963; Proctor, 1968; Clark, 1984; Wallace and Morris, 1986; Bredehoeft et al., 1992; Haneberg, 1995; Catchings et al., 1999; 2006; 2009; 2013; *in review*), groundwater ponds around subsurface faults and depending on the level of saturation, Vp in the fault zone can be similar or higher in velocity than the host rocks (Catchings et al., *in review*). The lack of a P-wave, low-velocity fault zone (which is usually characteristic of fault zones) occurs in saturated or partially saturated materials with Vp < 2,500 m/s (Catchings et al., *in review*). Multiple empirical studies have shown that the depth to the top of groundwater in Vp tomographic imaging correlates with velocities of about 1,500 m/s (Catchings et al., 1999; 2009; 2013; *in review*) and can provide evidence for faulting and ponding in the subsurface.

Seismic Refraction

Seismic refraction methods directly measure the time required for a seismic wave to travel from a source to a sensor at a known location. By knowing the distance between the source and the receiver (d) and the travel time (t), the velocity can be directly calculated ($v = d/t$). Because the first arrival on a seismogram is typically the refracted arrival, first arrivals can be used to determine the average velocity of subsurface materials between a source and a receiver for a given depth range (Figure 7). In using the tomography method, the average velocity from multiple source-receiver pairs is determined so that the average velocity at a given depth is calculated numerous times. This process provides for a highly accurate measure of the velocity at which seismic waves propagate through the subsurface. Empirical and laboratory studies have shown that various rock types have a range of seismic velocities depending on the physical condition (weathered, fresh, saturated, fractured, depth of burial/pressure, etc.) of the rocks and sediments (Christensen, 1966). As a result, refraction velocities can be used to differentiate among various types of subsurface materials. For example, unconsolidated sediments typically have much lower velocities than consolidated sediments; saturated sediments typically have much higher velocities than unsaturated sediments; fractured rocks typically have much lower velocities than comparable unfractured rocks.

One requirement of this method is that the subsurface layers must increase in seismic velocity with depth (for example, see Steeples and Miller, 1990), which is usually the case in the Earth. Where velocity varies both vertically and horizontally, seismic refraction tomography techniques can be used to create velocity models and allow for comprehensive interpretation. Near-surface velocity data are important because the greatest variations in seismic velocities typically occur near the surface, due to lateral variations in the composition and the physical state of the subsurface (Catchings et al., 2001). Although there can be overlap in velocity among various subsurface materials, velocity data (particularly when both P-wave (Vp) and S-wave (Vs) data are available) in combination with other geologic data, can be used to infer rock types and physical conditions in the subsurface. The refraction tomography method is particularly well-suited to imaging fault zones because the faulting process damages the host rocks, and the damaged rocks are typically lower in seismic velocity relative to the host rocks, providing a wide range of velocities to be imaged. Refraction data can also be used to develop reflection images (see for example, Catchings et al., 1998). This process is discussed in greater detail below.

Seismic Reflection

Seismic reflection methods are used to develop images of the subsurface using seismic energy that reflects from various horizons within the subsurface. The reflected seismic energy typically arrives after the refracted energy. The seismic reflection technique depends on acoustical impedance contrasts that typically occur at boundaries between geologic layers (for example, see Steeples and Miller, 1990). By using seismic reflection techniques, it is possible to image subsurface formations under the right conditions. This is done by measuring the amplitudes and travel times of seismic waves to return to the surface after reflecting off interfaces between layers with different physical properties.

In the subsurface, structural features and variations in layering are indicated by reflection times from several places on the surface. Multiple reflection points are recorded from a single subsurface interface (Dobrin and Savit, 1988). The common-depth-point technique is employed to record multiple signals associated with one single reflection point in the subsurface at multiple shot and receiver positions (Figure 8; Dobrin and Savit, 1988). These signals are then composited (i.e., stacked) during data processing to produce depth images of the subsurface. The amplitudes of the reflected waves, as a function of time, are used to infer subsurface layering and to create an image resembling a cross section through the Earth (for example, see Sleep and Fujita, 1997). Typically, seismic reflection imaging of fault zones is successful where faults vertically offset sub-horizontally layered units, where faults bisect rocks with marked differences in reflectivity, or where the fault is inclined at a low angle to the surface. However, in less than ideal conditions for reflection imaging, such as laterally discontinuous and highly faulted and folded strata that exists in my study area, seismic reflection alone cannot be used effectively to image faults (Catchings et al., 2013). As a result, I employed seismic refraction methods to measure detailed velocities at greater depths.

Vp/Vs Ratios and Poisson's Ratio

Faulting of rocks causes a greater reduction in Vs than in Vp, and the ratio of Vp to Vs can be diagnostic of fault zones (Catchings et al., 2013). High Vp/Vs ratios (>6) are indicative of fault zones, and can suggest a high level of saturation (Catchings et al., *in review*). In my study, the Vp and Vs refraction tomography models were developed independently using first arrivals from co-located sources and receivers. Both of the models are well constrained with identical parameters; they were then used to develop a tomography model of Vp/Vs ratios along the seismic profile by dividing Vp by Vs at each grid point of the velocity model. Because Vp/Vs ratios are calculated on the basis of both P-wave and S-wave data, the Vp/Vs ratio model was calculated only to the maximum depth of the Vp model because P-waves typically propagate to shallower depths than S-waves for a given source-receiver offset (Catchings et al., 2013). The shape of the model's contours can also provide evidence for faulting, and where Vp/Vs values peak, the dip can be used to infer fault dip.

Poisson's ratio, which is a measure of the amount of extension to the amount of compression, is calculated using the modeled Vp and Vs with the following calculation from Thomsen (1990):

$$\nu = E/2\mu - 1 = (3K-2\mu)/(6K+2\mu) = ((Vp/Vs)2 - 2)/2((Vp/Vs)2-2) \qquad (3)$$

where ν is Poisson's Ratio (Poisson's ratio),
μ is shear modulus (ratio of stress to strain),
E is Young's modulus (measure of stiffness of an elastic material),
K is bulk modulus (measures material's resistance to uniform compression),
Vp is P-wave velocity, and
Vs is S-wave velocity.

Poisson's ratio provides useful information about shallow groundwater saturation and faulting because large increases in Vp and Poisson's ratio can be caused by groundwater saturation of near-surface sediments (Catchings et al., 2013), and faults characteristically form barriers to the flow of groundwater (Tolman 1937; Dutcher and Garrett, 1963;

Proctor, 1968; Clark, 1984; Wallace and Morris, 1986; Bredehoeft et al., 1992; Haneberg, 1995; Catchings et al., 1999; 2006; 2009; 2013; *in review*). Poisson's ratio can vary from 0 to 0.5 for most materials; 0.5 is typically the Poisson's ratio of a fluid, and values are often locally high within fault zones (Catchings et al., 2013). Water saturation has little effect on S-wave velocities but does have a significant effect on Vp (Catchings et al., 2013). Typical crustal rocks have a Poisson's ratio of 0.2 to 0.3, but water-saturated sediments and rocks can have considerably higher Poisson's ratio values, and quartz-rich rocks can have considerably lower Poisson's ratio values (Catchings et al., 2013). Near-surface rocks typically have a relatively high Poisson's ratio due to the high water content below the vadose zone, and empirical studies have shown that a Poisson's ratio of about 0.44 in the near-surface correlates with the top of groundwater (Catchings et al., 2006). Values higher than 0.44 are typically highly water-saturated sediments and rocks (Catchings et al., 2013).

Data Acquisition

In June 2012, with assistance from USGS personnel and volunteers, I acquired a 60-m-long combined high-resolution seismic refraction and reflection survey near the Filoli Center in Woodside, California, just south of the Upper Crystal Springs Reservoir (Figures 4 and 9). The profile was oriented NE–SW, approximately perpendicular to the trend of the SAF and centered on the main 1906 surface rupture (Figure 4). Data acquisition and processing were the same as those used by Catchings et al. (2013), as described below. Because my study site was located on the property of the San Francisco Public Utilities Commission (SFPUC), I was required to obtain permits for the seismic survey, and the permit was valid only along existing roads. Thus, the seismic profile length and orientation were limited to the 60-m-long profile shown in Figures 4 and 9. The shots (seismic sources) were spaced laterally every 1 m to produce P- and S-wave data (Figure 9). The recording instruments were 40-Hz, single-element, Mark Products L-40A™ geophones that were co-located with each shot location. Each recording site and shot was measured using a meter tape and flagged to obtain the proper spacing. GPS locations for each geophone and shot were obtained using a handheld Trimble Geox (GeoExplorer). P-waves were generated using a steel plate and direct (vertical) hammer impacts onto the steel plate located on the ground surface (Figure 10). S-waves were generated by striking an aluminum block (with cleats to add shear to the surface) on each end multiple times using a 4.5 kg hammer. The impacts forced the block to move perpendicularly to the seismic profile (Figure 11).

The useful data recorded included P-wave refracted arrivals, P-wave reflections, and the corresponding S-wave arrivals. Approximately 2 seconds of data were recorded using a Geometrics Strataview™ RX-60 seismograph, with 60 active channels. The data were stored on the computer hard drive of the seismograph during acquisition and were later downloaded to a 4-mm tape for permanent storage in SEG-Y (Society of Exploration Geophysicists Y) format. Each geophone response to a single shot is known as a trace (wiggle), and the record of all traces for one shot is known as a shot gather (Figure 7). These shot records are shown in terms of time (ms) vs. channel number along the profile (measured in meters), which is also the distance (m) for this profile. This study, with 60 shot locations, produced 60 shot gathers, one for each shot, with 60 traces on each shot. Thus, approximately 3,600 first arrivals were used to generate the velocity models. The geophones remained fixed while each type of seismic source was 'shot' (impacted) along the profile. As a result of this acquisition layout, both refraction tomography and reflection data were generated from the same data sets.

Seismic Data Processing

The refraction data were initially processed on an interactive seismic processing package (ProMAX™), and first-arrivals were measured to within a few milliseconds. The first arrivals were then used to calculate seismic velocities using the code of Hole (1992). The reflection data were processed (also on ProMAX™) using only the P-wave reflections and several editing steps were taken to maximize the seismic signal. All of the processing work was done at the USGS in Menlo Park, California.

Seismic Refraction Processing

Refraction data were processed using a seismic tomographic inversion method (Hole, 1992) whereby P-wave first-arrival travel times on the traces of each shot gather are used to measure detailed velocities (Figure 7). The velocities derived from this method are used to develop velocity images (seismic tomography models) of the subsurface. This process was used for both P- and S-wave first-arrival travel times.

To create the velocity models using the P- and S-wave first-arrival refraction data, a modified version of Hole's (1992) refraction-tomography algorithm was used. Seismic tomography mathematically models the travel times of P- and/or S-wave data to map velocity contrasts in the subsurface of the Earth. This is an iterative method that uses 2-D ray tracing of first-arrival times through a gridded starting velocity model to match observed and calculated first-arrival travel times until a suitable fit is obtained for all arrivals from all shots (for example, see Hole, 1992). Ray tracing is used to calculate the path seismic waves travel through the subsurface back to the source by computing a raypath through a given velocity model (for example, see Hole, 1992). Travel times are determined from calculated raypaths for each wave front, and these times are compared with observed times (for example, see Hole, 1992). The model is continuously adjusted throughout the process to improve the equivalence between the observed and computed times until a realistic model is produced that agrees with known travel time data (for example, see Hole, 1992).

To create the tomographic models, mathematical inverse methods are used to develop statistically optimal solutions for ray paths directly from the first arrival data (Sleep and Fujita, 1997). These models are composed of a grid with specified velocities at certain grid points with interpolations in between (Hole, 1992; Sleep and Fujita, 1997). This grid allows for the subsurface to be divided into "boxes", and the many raypaths that travel through these boxes are computed to derive the velocities for the model (for example, see Sleep and Fujita, 1997). The greater the number of raypaths that travel through a given box, the better solution the final model will provide. Regions of the model that include an insufficient number of rays can lead to computational artifacts in the form of single-cell high-amplitude anomalies (Hole, 1992; Sleep and Fujita, 1997; Kissling et al., 2001).

The velocity models produced from this study were parameterized using a suitable grid (1 m x 1 m) to simulate real Earth structure and produce the highest resolution possible in the data set. The grid parameters were determined by the survey set up, including the length of the line, and the maximum reasonable depth (~30 m) that the model could resolve with accurate velocities. Different starting velocity models were developed that constrained the values for velocity at the top of the model, at the bottom of the model, and at specific grid nodes to account for enough differing vertical variations in velocity. The data were then traced to fit within these governing velocities. For each starting velocity model, 40 successive versions were also developed through an iterative process. Successive iterations display less smoothing of the velocity structure based on misfits, resulting in more jagged velocity contours and anomalies. Regardless of the starting model used, each inversion yielded similar final velocity models, suggesting that the velocity structure is well resolved. When deciding which models were best, 20–30 iterations for each model were ranked by image resolution and clarity.

Seismic Reflection Processing

Producing P-wave seismic reflection images requires the P-wave reflections and a suitable velocity model. Reflection data were processed using ProMAX™ to create an image of the subsurface that resembles a geological cross section of the Earth. To process the reflection data and maximize the signal of the seismic data that illustrate subsurface geologic features, the following steps were used (as per Catchings et al., 1999 and Catchings et al., 2001):

Geometry Installation

The survey layout, including the lateral distances and elevations for the shots and geophones were recorded using a handheld Trimble Geox (GeoExplorer) and then input into ProMAX™ to define the geometry of the profile.

Trace Editing

In the survey record, noise can be present in the form of undesired ground motion that can result from waves travelling along the Earth's surface or from scattered and diffracted waves reflecting off of surface or subsurface irregularities (Dobrin and Savit, 1988). Traces that were too noisy, either due to bad coupling between the geophone and the ground surface, malfunctioning geophones, or cultural noise, were edited to remove the noise. Not all noisy traces were present on all shot gathers, so independent editing was done for each shot gather.

Bandpass Filtering

To enhance the desired signal and attenuate noise, the frequency-phase content of the data was adjusted (Dobrin and Savit, 1988). To analyze the data properly, a bandpass filter was used to remove undesirable seismic data such as shear waves and cultural noise of specific frequencies. This filter essentially passes frequencies within a certain, desirable range containing coherent energy, while removing any frequencies that are outside of that range that is assumed to be noise with no useful reflection information (Dobrin and Savit, 1988).

Amplitude Correction

Amplitude adjustments attempt to correct the amplitude decay with time associated with spherical divergence and energy dissipation of seismic energy in the Earth (Dobrin and Savit, 1988). An Automatic Gain Control (AGC) was used to scale the amplitudes to be nearly alike across the entire data set.

Timing Corrections

When the shot electronically triggers the seismograph to record data, there is a small (~2 ms) delay between the actual trigger and the shot. A constant 2 ms was removed from the start time of each trace on every shot gather to account for this delay.

Velocity Analysis

To create the most accurate seismic reflection image possible, the modeling software has to make assumptions about the velocities in the subsurface. The velocities in the near subsurface (~1 m to ~20 m) were determined using the Vp refraction tomography model. Velocities in the deeper section were estimated using previous seismic studies and knowledge of the local geology.

Moveout Correction

The arrival time of a reflection increases with offset, which is the distance between the seismic source and the receiver, due to the greater length of the travel path (Dobrin and Savit, 1988). Due to the increasingly greater travel times of the seismic waves at the sensors, there is a delay for each seismic arrival, known as moveout. To accurately sum (stack) the data at each common-depth-point (CDP), a moveout correction was applied using velocities obtained during the velocity analysis. This correction produces a seismic image such that all of the reflections on each trace are represented as if the traces were recorded at the source (zero time) (Burger et al., 2006).

Muting

When making seismic reflection images, only the P-wave reflections are of interest. To remove refractions, as well as surface and air waves that were not completely removed through filtering, mutes were applied to the data before and after stacking.

Stacking

As mentioned earlier, the CDP technique is used to strengthen the data and minimize the noise. This technique involves organizing the seismic survey so that there are many shots and receivers along the profile. Because of this arrangement, signals associated with a given reflection point in the subsurface are recorded through a number of different shot and geophone pairs (Dobrin and Savit, 1988). These shot-geophone pairs therefore have CDPs, but varying offsets. Each shot-geophone pair produces its own reflection. After correcting the data, all reflections were stacked, which means the signals for each coincident subsurface reflection point (CDP) were added together (Dobrin and Savit, 1988).

Depth Conversion

Because my seismic reflection data were not migrated, the travel times were converted to depth based on the Root Mean Square (RMS) velocities converted from the velocity analysis described earlier. The RMS velocities are the difference between the model's predicted measurements and actual observed values (for example, see Burger et al., 2006).

Migration

In the presence of many faults and varying rock types in the subsurface, diffraction hyperbolae are abundant in the reflection image. To correct for this, a mathematical process is employed that moves seismic energy back to where the event occurred in the subsurface as opposed to the location it was recorded at the surface. However, the reflection image presented within this report is unmigrated because little was resolved after this correction due to the complex geology.

RESULTS

This study produced multiple tomographic velocity models and a reflection image detailing the subsurface structure of the Peninsula segment of the SAFZ, the results of which are discussed below.

P-wave Velocity Model

P-wave velocities range from about 600 m/s at the surface to more than 4,000 m/s at depths of about 20 m below the ground surface (Figure 12). The 1,500 m/s velocity contour (white line in Figure 12), has been shown by previous empirical studies to correlate with the depth to the top of groundwater (Catchings et al., 2000; 2013), implying that the top of static groundwater is about 3–7 m below the ground surface along most of the seismic profile (Figure 12). In the subsurface, abrupt vertical variations in the depth to groundwater often correlate with subsurface faults that act as barriers to groundwater flow (Tolman 1937; Dutcher and Garrett, 1963; Proctor, 1968; Clark, 1984; Wallace and Morris, 1986; Bredehoeft et al., 1992; Haneberg, 1995; Catchings et al., 1999; 2006; 2009; 2013; *in review*). The top of groundwater is vertically offset by about 3 m at distance meters 38, and 52 of the seismic profile (Figure 12). The trace observed at meter 52, however, may not be real due to possible edge effects. At each of these locations, there is near-surface thickening of low-velocity rocks, an abrupt vertical step in the 1,500 m/s velocity contour (top of groundwater) and marked lateral variations in the higher velocity rocks at depth (more pronounced low-velocity zones). At distance meters 38 and 52, P-wave velocities deepen to the northeast (Figure 12). At meter 18, though there is no abrupt step in the groundwater contour, there are steps in the velocity contours at depth, which may suggest the presence of an additional fault trace below the top of groundwater (Figure 12). The main 1906 surface rupture is located at distance meter 38, which correlates with the location determined in previous paleoseismic studies (Zachariasen et al., 2011). Groundwater normally flows from areas of higher elevation to lower elevation, which is southwest to northeast in my immediate study area. The level of groundwater appears to pond between distance meters 5 and 35, likely due to the SAF acting as a groundwater barrier. The high level of groundwater saturation likely contributed to the observed localized high Vp in the upper 20 m. A high-velocity zone

(>2,300 m/s) that widens with depth is located at the center of the profile between distance meters 20 and 30 (Figure 12). This high-velocity zone may correlate with the main fault zone at depth that appears to be bounded by the main 1906 fault trace and a possible secondary fault trace at about distance meter 18. It is also likely that this high-velocity zone could be correlated with another fault trace at depth that does not appear to reach the ground surface. Looking closely at the velocity model, there is a very small slope in the 1,500 m/s groundwater contour at meter 25 that suggests there is some structure beneath the surface, but it does not appear to extend to the surface. The highest velocities observed in this zone (>3,000 m/s) have been shown in previous studies to correlate with both well-lithified sediments and fractured or unfractured crystalline rock, which could be the materials at depth at the study site.

Borehole

To investigate the subsurface materials, a 6-m deep borehole was hand-augered into the high velocity zone at distance meter 25 of the profile (Figure 12). The upper 1.5 m contained unconsolidated sediments with very low moisture content (Figure 13). Water was reached at a depth of about 3 meters, which correlates well with the 1,500 m/s contour on the Vp model (Figure 12) and with the depth to the top of groundwater observed in paleoseismic trenches (Zachariasen et al., 2011). Through the upper section of the borehole (upper ~4.5–5 m) there was coarse gravel mixed with variably colored clay containing rock fragments. The lowest 1 m or so of the borehole comprised extremely compact, moist blue clay (Figure 13), which could be altered bedrock. The bright blue color of this clay suggests it may have originated from serpentinite that was sheared during fault movement (R. Catchings and M. Rymer, pers. comm. 2013), which may be the cause of such high P-wave velocities. A very small slope can be seen in the 1,500 m/s groundwater contour on the Vp model (Figure 12), further suggesting that a fault trace containing sheared serpentinite may exist at this location, though it probably does not break Holocene sediments.

S-wave Velocity Model

Along the profile (Figure 14), S-wave velocities range from about 300 m/s at the surface to about 800 m/s at a depth of about 20 m below ground surface, with the lowest velocities concentrated in the vicinity of the main 1906 SAF trace. Because fluids do not affect S-wave velocities as significantly as P-wave velocities, the Vs model predominantly shows the effects of shearing and the velocity contours are indicative of subsurface structure. Near-surface S-wave velocity contours are highly variable, with abrupt lateral changes that display complex structures likely associated with the highly variable rock and sediment types at depth. The materials with the lowest S-wave velocities extend from about distance meter 20 to the northeastern most end of the profile, where the low-velocity material reaches a maximum thickness of 7 m at distance meter 38. This location (distance meter 38) is the known location of the 1906 surface rupture (Figure 14). At distance meter 38, minima of the velocity contours can be connected along the fault trace, suggesting that the main 1906 fault trace may dip to the southwest at an average dip of about 75° in the upper 10 m (Figure 14). At distance meter 18, there is a thin low-velocity zone at the surface, and vertical steps in the velocity contours at depth that may correlate with a secondary fault trace that dips to the northeast. Northeast of the main 1906 SAF trace, S-wave velocity contours appear to flatten, with a slight deepening of velocities and steps in the velocity contours at distance meter 52 (Figure 14). Connecting the minima of these contours suggests another secondary fault trace here with a southwest dip. The lowest velocity material likely correlates with Holocene sediments of the fluvial plain on the northeast of the profile, whereas the higher velocity sediments on the southwest likely correlate with the older rocks that lie on the hill slope, immediately southwest of the seismic line.

Vp/Vs Ratios

The highest Vp/Vs ratios (Figure 15) range from 6 to 7.5 at depths of 5–20 m between distance meters 22 and 38 of the profile, suggesting a highly saturated, possible fault zone at depth immediately southwest of the main 1906 trace. This area of the model likely coincides with a fault zone at depth because of the high Vp (high levels of water saturation), and low Vs (shearing). As discussed earlier, in regions where subsurface materials are highly saturated, high Vp can disguise what normally should be a P-wave, low-velocity fault zone. Vp/Vs ratios, therefore, are a significant asset when used for modeling fault zones in regions that display these characteristics (Catchings et al., *in* *review*). The high Vp/Vs ratios seen here do not extend to the surface or shallower than the 1,500 m/s velocity contour observed on the Vp model (upper 3 m), further suggesting that if this is a major fault trace that extends up through these high values, it probably does not break the youngest sediments (Figure 15). The southwest dip of the peak Vp/Vs values suggests that the main SAF dips about 75 degrees to the southwest in the upper 20 m. There are other areas that show significant lateral variations, mostly at depths greater than 15 m. Other probable fault zones inferred from the previously discussed velocity images and can be seen at distance meters 18 and 52 where there are slight lateral variations (Figure 15).

Poisson's Ratio

Poisson's ratio along the profile were developed from the modeled Vp and Vs for each grid point (Figure 16). Poisson's ratio is useful in seismic imaging because it can provide information about groundwater saturation and faulting. Poisson's ratio typically ranges between 0.2 and 0.5 for most materials, with a Poisson's ratio of 0.5 correlating with liquid (Catchings et al., 2013; *in review*). Empirical studies have shown that saturated materials can have Poisson's values greater than 0.44 in the near surface, and values are often locally high over fault zones (Catchings et al., 2013; *in review*). Along the profile, Poisson's ratio ranges from about 0.26 to about 0.48 (Figure 16). Relatively high near-surface Poisson's ratios (>0.44) occur between distance meters 20 and 40, with the highest Poisson's ratio values occurring at depth in the center of the profile above the P-wave, high-velocity zone (Figure 16). This high Poisson's ratio area coincides approximately with the depth to the 1,500 m/s P-wave velocity contour, further suggesting that high Poisson's ratio values are associated with groundwater saturation. I interpret the high Poisson's ratio values near distance meter 25 of the profile to be a secondary fault trace. The relatively high values coincide with zones of faulting inferred from other images, as well as areas with significant lateral variations in Vp and Vs seen at distance meter 52 (Figure 16).

Reflection Section

A reflection image was developed by stacking secondary arrivals from each shot gather (Figure 17). To stack these P-wave reflection data, the Vp tomographic model was converted to an interval velocity model. Because the Vp model did not give velocities at all depths along the profile, the Vp model was linearly extended laterally and vertically in the upper 20 m. Below 20 m, velocities were estimated using 1-D velocity estimates.

Continuous reflections on the images are taken to correlate with layer boundaries with differences in density and/or seismic velocity, and discontinuities can be used to infer faults (for example, see Burger et al., 2006). Diffractions on a seismic section are recognized as a hyperbolic curve and occur when seismic energy radiates from an abrupt termination of structure, such as a fault (for example, see Burger et al., 2006). The dip of a fault can also be inferred by using the location of the apices of multiple diffraction hyperbolae (Catchings et al., *in review*).

A stacked seismic reflection image of the upper 200 m (Figure 17) shows several reflectors in the upper 20 m, although it is not possible to trace these reflectors continuously across the profile. The reflection image also contains multiple horizons of strong reflections in the upper few meters, with the strongest reflections occurring southwest of the main 1906 surface rupture. There are few laterally continuous reflections observed along the profile, probably because of the deformed and complex local geology. The reflections are approximately horizontal on the northeastern end of the profile, whereas reflections appear to have a slight downward curvature on the southwestern end of the profile near distance meter 15 (Figure 17). The only area with continuous reflectors is near the northeast in the upper few meters, which may correlate with unconsolidated Holocene sediments.

Strong, near-vertical diffractions are observed at meters 25 and 38 of the profile (Figure 17). Alignments of these diffractions that extend through the reflection image at these locations suggest the presence of notable faults. While diffractions can be generated by structures other than faults, the fact that they are aligned near-vertically suggests they were generated by faults along the profile. At meter 38, the location of the main 1906 surface rupture, the apices of these diffractions are located progressively to the southwest, suggesting the fault dips toward the southwest. The strongest diffractions are centered at about distance meter 25 at depths greater than 50 m beneath the P-wave, high-velocity zone, further suggesting that the high-velocity zone (at distance meter 25 at the ground surface) is related to faulting and that there may be a major fault trace at depth (Figure 17). The diffractions on either side of this area appear to meet those in the middle, especially the diffractions beneath the main 1906 fault trace at distance meter 38, suggesting that the fault traces here may merge at depth (Figure 17, B).

DISCUSSION

Analyses of the P- and S-wave data provide details of the near-surface structure of the 1906 surface rupture zone of the SAFZ and can be compared with previous geophysical and paleoseismic studies in the study area. Implications for re-evaluating slip rates on the Peninsula segment of the SAFZ, and suggestions for future work, are also discussed.

Interpretation of the Near-Surface San Andreas Fault Zone

Based on the location of a near-surface low-velocity zone at about distance meter 38 of the Vs model (Figure 14) and corresponding highs in the Vp, Vp/Vs and Poisson's ratio (Figures 12, 15 and 16, respectively), I suggest that the main 1906 SAF surface rupture zone is located at distance meter 38 of the seismic profile. High levels of groundwater saturation are expected on the uphill side of faults (towards the southwest in this study) because faults can act as barriers to groundwater flow and groundwater usually flows downhill (Catchings et al., 2013; *in review*). Vertical offsets in the 1,500 m/s velocity contour, which indicate the depth to the top of groundwater, can indicate fault traces in the subsurface. In the Vp model, the 1,500 m/s P-wave velocity contour can be traced across the entire model (Figure 12). Between distance meters 7 and 38, groundwater levels seem to be the shallowest, suggesting a localized zone of shallow depth to the top of groundwater that is centered directly over the high-velocity P-wave zone. The top of groundwater, shown by the 1,500 m/s P-wave contour, is vertically offset by about 3 m at distance meter 38 (Figure 12), suggesting that the fault acts as a barrier to groundwater flow. Numerous studies on other faults have shown that faults are generally barriers to ground water flow (Tolman 1937; Dutcher and Garrett, 1963; Proctor, 1968; Clark, 1984; Wallace and Morris, 1986; Bredehoeft et al., 1992; Haneberg, 1995; Catchings et al., 1999; 2006; 2009; 2013; *in review*). Abrupt vertical variation in the depth to the top of groundwater, as inferred from Vp contours at distance meter 52 (Figure 12), is also consistent with at least one possible secondary fault traces in the near surface. At distance meter 18 of the seismic profile, there are steps in the velocity contours at depth, and though there is no abrupt offset in the groundwater contour, this may be indicative of a more permeable fault in the near-surface. Along the Vp profile, a slight near-surface thickening of low-velocity rocks can be seen at each of these locations, consistent with faulting (Figure 12).

Evidence for these secondary fault traces within the Vs model include low-velocity zones and vertical steps in the velocity contours (Figure 14). On the Vs model, low-velocity zones are slightly more apparent at these locations, and I interpret the dips of the fault traces on the basis of the minima of the velocity contours. The Vs model also provides detailed insight into the subsurface structure, as near-surface S-wave velocity contours vary abruptly across the profile, especially near the interpreted fault traces and particularly at distance meter 38 (Figure 14).

Most empirical P-wave refraction tomography studies have shown a lack of a near-surface, P-wave, low-velocity fault zone, particularly in rocks and sediments with Vp less than about 2,500 m/s (Catchings et al., *in review*). In these conditions, both the saturated fault zone and adjacent host rocks can have similar Vp ranging from about 1,500 m/s to 2,500 m/s (Catchings et al., *in review*). At greater depths (>10 m), however, rocks are more compacted and higher in velocity (>2,500 m/s), and the saturated host rocks typically have higher Vp than the adjacent saturated faulted rocks (Catchings et al., 2013). The Vp model shows a relative high-velocity zone centered at distance meter 25 of the seismic profile that widens with depth, bounded between a possible secondary trace at distance meter 18 and the main 1906 fault trace at meter 38 (Figure 12). This high-velocity zone appears to mask the low-velocity areas presumably located beneath the fault traces. This high-velocity zone could also be related to the main fault zone at depth. I interpret this high-velocity zone as originating from a significant fault trace at this location that does not appear to break the surface. This trace is likely an older fault that may be associated with long-term movement prior to the main 1906 break and is expressed as vertically oriented high-velocity material, possibly serpentinite. The highest Vp/Vs ratios (>6), which are indicative of subsurface faulting, directly coincides with the P-wave, high-velocity zone, further suggesting this is a fault zone, which may widen at depth. The highest Poisson's ratios (Figures 16) also coincide with the P-wave, high-velocity zone suggesting that the fault zone is highly groundwater saturated.

The seismic reflection image (Figure 17) contains evidence consistent with the interpreted fault pattern based on the Vp, Vs, Vp/Vs, and Poisson's ratio tomography models. At each of the fault trace locations (distance meters 18, 38, and 52), there appear to be vertically offset reflectors and diffraction hyperbolae. Diffraction hyperbolae in the reflection image approximately align beneath the interpreted fault traces and the strongest diffractions are observed directly beneath the zone of high P-wave velocities and the highest Vp/Vs ratios at distance meter 25 of the seismic profile. The diffractions on either side of this zone also appear to meet those in the middle, suggesting that the fault traces here may merge at depth. The P- and S-wave velocity models, along with the Vp/Vs ratios model were each superimposed on top of the reflection image for further interpretation (Figure 18). The low-velocity, S-wave material in the upper few meters on the northeast portion of the profile, which are likely unconsolidated sediments, appears to correlate with the relatively continuous reflections here (Figure 18, B). The P-wave, high-velocity zone, and the highest Vp/Vs ratios correlate with the strongest diffractions on the reflection image at depth, further implying this is a fault zone (Figure 18, A and C, respectively). There likely is a significant fault beneath this area, but that fault does not appear to break the surface based on the change in slope in the 1,500 m/s contour. About 5 m of deposition overlies the diffractions here, suggesting this fault may be much older than the 1906 surface rupture and may have previously been taking up slip on the SAFZ prior to the 1906 rupture.

The borehole hand-augered into the high-velocity zone at distance meter 25 (Figure 12) encountered water at about 3 m, suggesting that the 1,500 m/s contour is a good indicator of groundwater level. The uppermost ~2 m contained unconsolidated sediments (Figure 13), consistent with the low S-wave velocities observed on the Vs model (Figure 14) and the continuous reflectors on the reflection image (Figure 17). Below these sediments, the borehole revealed coarse gravel mixed with variably-colored clay containing rock fragments. This gravel likely originated from Santa Cruz mountains sediments deposited by Spring Creek (Figure 4). Extremely compact, moist blue clay was found throughout the rest of the borehole (Figure 13). This type of clay has been seen in previous studies to be derived from serpentinite that has been sheared through fault movement (R. Catchings and M. Rymer, pers. comm. 2013).

Comparison with Previous Geophysical Studies

There are few geophysical investigations of the subsurface structure of the Peninsula segment of the SAF and the profile presented within this thesis is one of the few available high-resolution seismic images that can be compared with observations from nearby studies by Catchings et al. (2013; *in review*).

Catchings et al. (2013) acquired and analyzed high-resolution seismic refraction data from near San Andreas Lake, approximately 15 km northwest of my study location (Figure 1, number 1). The methodology used to acquire and process the seismic data in my study is identical to that used by Catchings et al., (2013; *in review*); therefore, the results presented here are internally consistent with previously published results of similar studies. Catchings et al. (2013) acquired three seismic profiles that showed complex subsurface faulting within about 100 m of the main 1906 SAF trace. They correlated at least three additional near-surface fault traces located within about 20 m of the main 1906 surface rupture to previously mapped traces and found that the width of the main fault zone appears to vary slightly with location (Catchings et al., 2013). The locations of these additional fault traces correlate well with the locations of possible fault traces found in my study. In a separate study, Catchings et al. (*in* review) conducted a similar study between San Andreas Lake and Lower Crystal Springs reservoir, and they found similar Vp, Vs, Vp/Vs and Poisson's ratio values along the 1906 surface rupture zone of the SAF. Thus, similar variations in P- and S-wave velocities and abrupt changes in the depth to the top of groundwater across the fault traces were found in each study in the area.

Comparison with Previous Paleoseismic Work

Previous paleoseismic work has accurately located the main 1906 fault trace of the Peninsula segment of the SAF (Hall et al, 1999; Prentice and Moreno, 2007; Prentice et al., 2008; Zachariasen et al., 2011) and its location can be projected to my seismic profile at distance meter 38. All of my velocity models (Figures 12, 14 through 16) are consistent with the 1906 fault trace at distance meter 38. Zachariasen et al. (2011), whose work was done at my study site (Figure 4), observed a main zone of faulting concentrated within 2 m of the main 1906 fault trace; but these mapped traces do not appear to break the ground surface or units within about 2 m of the surface (Zachariasen et al., 2011). Their observations are consistent with my reflection image (Figure 17), which shows mostly continuous reflectors in the near-surface (upper 2 m) across the entire profile that do not seem affected by faulting at distance meters 38 and 52. At the site, sediments observed at depth include sheared gravel, sand, and silt, as well as channel gravel and colluvial-wedge rubble and clay (Zachariasen et al., 2011). The discontinuous reflectors and lateral variations in velocities seen in my seismic images can be attributed to the strata seen in these cross-fault trenches by Zachariasen et al. (2011). Within the fault zone, they observed units that were difficult to identify due to the extent of shearing and disturbance from faulting. Both trenches exposed fluvial channel and overbank deposits overlying highly weathered colluvium that is a dark grey deposit containing pebble-sized clasts (Zachariasen et al., 2011).

Implications for Seismic Hazard

Together, all of the seismic images suggest that there is at least one or more near-surface fault traces within about 25 m of the main 1906 surface rupture. A significant fault trace was observed just southwest of the main 1906 fault trace that does not appear to reach the surface. This trace may be associated with long-term movement prior to the main 1906 break. Based on previous observations of the 1906 rupture zone (Schussler, 1906), the secondary near-surface fault traces could also be capable of slipping during future earthquakes. Movement on multiple splays on a fault suggests that slip would be partitioned along several near-surface faults. In such a case, paleoseismic measurements made on a single fault trace would thus fail to capture the total slip during past earthquakes on the SAF. Furthermore, slip on subparallel fault traces can result in both local compressional and extensional movements (Catchings et al., 2013) that may not be accounted for in paleoseismic investigations. Slip consisting of both compressional and extensional movements previously occurred at the southern end of San Andreas Lake, where a manmade structure located between two faults was altered from a circular to a northwest–southeast-oriented oblong structure during the 1906 earthquake (Schussler, 1906). The individual fault traces observed at the surface may merge into a single fault zone at depth, creating a flower structure in the subsurface.

The large lateral and vertical variations in P- and S-wave velocities (Figures 12 and 14, respectively) imply complex subsurface structures that are associated with the highly variable sediment and rock types observed in paleoseismic trenches (Zachariasen et al., 2011). The rocks in my study area do not appear to be well stratified, as they do not generate strong reflective energy in the upper few tens of meters. The Vp model shows the majority of the lower P-wave velocity (1,000–3,000 m/s) material is concentrated in the upper few meters and at the ends of the seismic survey, beneath the inferred fault traces (Figure 12). Previous studies have shown that P- and S-wave velocities between 1,000 and 3,000 m/s can correlate with near-surface unconsolidated sediments, weathered sedimentary rock, and weathered Franciscan rocks (Catchings et al., 2002), as seen in the upper few meters of deposits at my study site.

Previous work has shown that subsurface materials with P-wave velocities between 3,300 m/s and 4,000 m/s can correspond to multiple rock types, such as consolidated sedimentary rocks and deeply weathered granitic rocks or Franciscan crystalline rocks (Christensen, 1966; Catchings et al., 2002). Salinian terrane granitic or Franciscan crystalline rocks have typical velocities greater than 4,000 m/s (Catchings et al., 2002). Because higher P-wave velocities correlate with either well-lithified sediments or highly fractured or deeply weathered crystalline rock, areas of the models with velocities greater than 4,000 m/s are harder to classify. Based on previous observations (Catchings et al., 2013; *in review*) and paleoseismic work (Zachariasen et al., 2011) in the area of this study, the higher velocities of the Vp model correlate with weathered Franciscan crystalline rocks, most likely serpentinite (Figure 12). This inference is further supported by the presence of blue clay found in augered samples at the very top of the P-wave, high-velocity zone (Figures 12 and 13).

Because my study found possible evidence for multiple fault traces in the SAFZ, it is possible that slip rates for the Peninsula segment of the SAF may only be minimal values. If slip on all of the faults within the fault zone is not measured, lower slip rates may be assigned to the fault that do not accurately characterize the slip history, and, therefore, the slip rate and recurrence intervals for the SAFZ in this area. If slip does not always occur on a particular fault trace, some of the earthquakes will not be recognized in paleoseismic studies. For example, if slip occurred on the "main" trace in 1906, but prior to that, slip was limited to one of the other traces, examining only the 1906 trace would provide little or no information about rupture prior to 1906. Assessing the newly inferred faults to see if they actually exist and, if so, were active within the Holocene, which would affect the overall slip rate at the site.

Suggestions for Future Work

The seismic survey presented in this study imaged the subsurface structure of the main 1906 fault trace in the study area, but only about 25 m on either side of the 1906 surface rupture were imaged. To better investigate the possible presence of additional near-surface fault traces or additional fault zones, further seismic studies should examine a broader area beyond the main 1906 surface rupture. The lateral extent of faulting and the fault geometry with depth can provide greater information about how the SAF ruptures during large-magnitude earthquakes. Further seismic work could also be done along other transects across the fault to determine the extent of additional fault traces. In acquiring the seismic data, I suggest that combined P- and S-wave refraction and reflection imaging be used to provide the most information about the geometry and rock types due to the geologic complexity encountered along the Peninsula segment of the SAF.

Furthermore, the borehole that was hand-augered only investigated one location along the seismic profile (Figure 12, distance meter 25) to a maximum depth of only about 6 m. To better constrain the lateral extent of the subsurface materials, in particular that of the blue clay, more locations along the seismic profile should be investigated and to greater depths. Locations on either side of potential fault traces should also be considered to determine the exact location of the groundwater level. In doing so, if there is a difference in the level of groundwater on either side of these locations, faults may be better identified.

CONCLUSIONS

I used coincident P- and S-wave data from a 60-m-long high-resolution seismic profile across the Peninsula segment of the SAF to develop refraction tomography Vp, Vs, Vp/Vs and Poisson's ratio images, and a P-wave reflection image of the shallow crust. Analysis of the images provide insight into the geometry and slip of the Peninsula segment of the SAF:

(1) The data indicate one or more near-surface fault traces within about 25 m of the main 1906 fault zone. A significant fault trace expressed as vertically oriented high-velocity material, possibly altered serpentinite, just southwest of the 1906 fault surface rupture may be associated with long-term slip on the SAF prior to the current main trace, which slipped in 1906. Investigating if these newly inferred faults actually exist and, if so, were active within the Holocene may affect the overall slip rate at the site.

(2) Observations consistent with the presence of multiple fault traces include: (a) high P-wave velocities (>2,300 m/s) and abrupt variations in P-wave velocity, particularly the 1,500 m/s velocity contour that indicates the depth to the top of groundwater, (b) S-wave low-velocity zones, (c) high Vp/Vs ratios, signifying high groundwater saturation and shearing in the subsurface, and (d) diffraction hyperbolae in the seismic reflection image, whose apices align to give apparent dips for these strands.

(3) Sub-parallel fault strands in the near-surface are of particular importance because these could produce differential movement resulting in complex shearing involving both compressive and extensional stresses. This suggests that slip may be partitioned among several near-surface faults.

(4) Large lateral and vertical variations in P- and S-wave velocities suggest a complex geometry of geologic units that are likely composed of high-velocity (3,000–4,000 m/s) Franciscan serpentinite.

While the findings presented within this report show considerable complexity associated with the Peninsula segment of the SAF, further work in the fields of geophysics and paleoseismology is needed to verify the existence of the inferred faults and, if so, to see if they reach the ground surface, which may help to better determine the slip rate along the Peninsula segment of the SAF.

REFERENCES

Aki, K., and Lee, W. H. K., 1976, Determination of three-dimensional velocity anomalies under a seismic array using P-arrival times from location earthquakes. I. A homogeneous initial model: Journal of Geophysical Research, v. 81, p. 4381–4399.

Argus, D.F., and Gordon, R.G., 2001, Present tectonic motion across the Coast Ranges and San Andreas fault system in central California: Geological Society of America Bulletin, v. 113, p. 1580-1592.

Atwater, T., 1989, Plate tectonic history of the northeast Pacific and western North America, *in* Winterer, E.L., Hussong, D.M., and Decker, R.W., eds., The Eastern Pacific Ocean and Hawaii: Boulder, Colorado, Geological Society of America, The Geology of North America, v. N, p. 21–72.

Bakun, W.H., 1999, Seismic Activity of the San Francisco Bay Region: Bulletin of the Seismological Society of America, v. 89, p. 764–784.

Baldwin, J., Prentice, C.S., Wetenkamp, J., and Sundermann, S., 2006, Preliminary earthquake record of the Peninsula section of the San Andreas fault, Portola Valley, California: Seismological Research Letters, v. 77, p. 248.

Baldwin, J., and Prentice, C.S., 2008, Earthquake records of the Peninsula segment of the San Andreas fault, Portola Valley, California: Collaborative research with William Lettis & Associates, Inc. and U.S. Geological Survey, Final Technical Report, U.S. Geological Survey National Earthquake Hazards Reduction Program Award Number 05HQGR0073, 41 p.

Brabb, E.E., Graymer, R.W., and Jones, D.L., 2000, Geologic map and map database of the Palo Alto 30' X 60' quadrangle, California: U.S. Geological Survey Miscellaneous Field Studies Map MF-2332, Scale: 1:100,000.

Bredehoeft, J.D., Belitz, K., and Sharp-Hansen, S., 1992, The hydrodynamics of the Big Horn Basin: A study of the role of faults: American Association of Petroleum Geologists Bulletin, v. 76, p. 530-546.

Burger, H.R., Sheehan, A.H., Jones, C.H., 2006, Introduction to Applied Geophysics: Exploring the Subsurface: New York, W.W. Norton & Company, Inc., 554 p.

Catchings, R.D., Goldman, M.R., Lee, W.H.K., Rymer, M.J., and Ponti, D.J., 1998, Thrust faults apparently related to and possible co-seismic origin of surface cracks in Potrero Canyon, Los Angeles County, California, following the 1994 Northridge, California, Earthquake: Bulletin of the Seismological Society of America, v. 88, p. 1379–1391.

Catchings, R.D., Gandhok, G., Goldman, M.R., Horta, E., Rymer, M.J., Martin, P., Christensen, A., 1999, Subsurface, high-resolution, seismic images from Cherry Valley, San Bernardino County, California: Implications for water resources and earthquake hazards: U.S. Geological Survey Open-File Report 1999-26, 57 p.

Catchings, R.D., Cox, B.F., Goldman, M.R., Gandhok, G., Rymer, M.J., Dingler, J., Martin, P., Christensen, A., and Horta, E., 2000, Subsurface structure and seismic velocities as determined from high-resolution seismic imaging in the Victorville, California area: Implications for water resources and earthquake hazards: U.S. Geological Survey Open-File Report 2000-123, 70 p.

Catchings, R.D., Saulter, D.E., Powars, D.S., Goldman, M.R., Dingler, J.A., Gohn, G.S., Schindler, J.S., and Johnson, G.H., 2001, High-resolution seismic reflection/refraction images near the outer margin of the Chesapeake Bay impact crater, York-James Peninsula, Southeastern Virginia: U.S. Geological Survey Open-File Report 2001-407, 18 p.

Catchings, R.D., Rymer, M.J., Goldman, M.R., Hole, J.A., Huggins, R., and Lippus, C., 2002, High-resolution seismic velocities and shallow structure of the San Andreas fault zone at Middle Mountain, Parkfield, California: Bulletin of the Seismological Society of America, v. 92, p. 2493–2503.

Catchings, R.D., Goldman, M.R., and Gandhok, G., 2006, Structure and velocities of the northeastern Santa Cruz Mountains and the western Santa Clara Valley, California, from the SCSI-LR seismic survey: U.S. Geological Survey Open-File Report 2006-1014, 78 p.

Catchings, R.D., Rymer, M.J., Goldman, M.R., and Gandhok, G., 2009, San Andreas fault geometry at Desert Hot Springs, California, and its effects on earthquake hazards and groundwater: Bulletin of the Seismological Society of America, v. 99, p. 2190–2207.

Catchings, R.D., Rymer, M.J., Goldman, M.R., Prentice, C.S., and Sickler, R.R., 2013, Fine-scale delineation of the location of and relative ground shaking within the San Andreas fault zone at San Andreas Lake, San Mateo County, California: U.S. Geological Survey Open-File Report 2013-1041, 58 p.

Catchings, R.D., Rymer, M.J., Goldman, M.R., Sickler, R.R., Criley, C.J., *in review*, A method and example of seismically imaging near-surface fault zones in geologically complex areas using Vp, Vs, and their ratios: Bulletin of the Seismological Society of America.

Chester, F.M., and Logan, J.M., 1986, Composite planar fabric of gouge form the Punchbowl fault, California: Journal of Structural Geology, v. 9, p. 621–634.

Chester, J.S., Chester, F.M., and Kronenberg, A.K., 2005, Fracture surface energy of the Punchbowl fault, San Andreas system: Nature, v. 437, p. 133–136.

Christensen, N.I., 1966, Elasticity of ultrabasic rocks: Journal of Geophysical Research, v. 71, p. 5921–5931.

Clark, M.M., 1984, Map showing recently active breaks along the San Andreas Fault and associated faults between Salton Sea and Whitewater River-Mission Creek, California: U.S. Geological Survey Miscellaneous Investigation Series Map I-1483, Scale 1:24,000.

d'Alessio, M.A., Johanson, I.A., Bürgmann, Schmidt, D.A., and Murray, M.H., 2005, Slicing up the San Francisco Bay Area: Block kinematics and fault slip rates from GPS-derived surface velocities: Journal of Geophysical Research, v. 110.

Dobrin, M.B., and Savit, C.H., 1988, Introduction to Geophysical Prospecting: New York, McGraw-Hill Book Company, 867 p.

Domenico, S.N., 1974, Effects of water saturation on sand reservoirs encased in shales: Geophysics, v. 29, p. 759–769.

Domenico, S.N., 1977, Elastic properties of unconsolidated sand reservoirs: Geophysics, v. 41, p. 882–894.

Dutcher, L.C., and Garrett, A.A., 1963, Geologic and hydrologic features of the San Bernardino area, California: U.S. Geological Survey Water Supply Paper, 1419, 114 p.

Flinn, D., 1977, Transcurrent fault and associated cataclasis in Shetland: Journal of the Geological Society of London, v. 133, p. 231–248.

Gupta, V., and Bergstrom, J.S., 1998, Compressive failure of rocks by shear faulting: Journal of Geophysical Research, v. 103, p. 23875–23895.

Hall, N.T., 1984, Holocene History of the San Andreas fault between Crystal Springs Reservoir and San Andreas Dam, San Mateo County, California: Bulletin of the Seismological Society of America, v. 74, p. 281–299.

Hall, N.T., Wright, R.H., and Clahan, K.B., 1999, Paleoseismic studies of the San Francisco Peninsula segment of the San Andreas fault zone near Woodside, California: Journal of Geophysical Research, v. 104, p. 23215–23236.

Hall, N.T., Wright, R.H., and Prentice, C.S., 2001, Studies along the Peninsula segment of the San Andreas fault, San Mateo and Santa Clara Counties, California, *in* Ferriz, H., and Anderson, R., eds., Engineering Geology Practice in Northern California: California Division of Mines and Geology, Bulletin 210, Special Publication 12, p. 193–210.

Han, D., Nur, A., and Morgan, D., 1986, Effects of porosity and clay content on wave velocities in sandstones: Geophysics, v. 51, p. 2093–2107.

Haneberg, W.C., 1995, Steady state groundwater flow across idealized faults: Water Resources Research, v. 31, p. 1815–1820.

Healy, J. and Peake, L., 1975, Seismic velocity structure along a section of the San Andreas Fault near Bear Valley, California: Bulletin of the Seismological Society of America, v. 65, p. 1177–1197.

Hole, J.A., 1992, Nonlinear high-resolution three-dimensional seismic travel time tomography: Journal of Geophysical Research, v. 97, p. 6553–6562.

Irwin, W.P., 1990 Geology and plate-tectonic development, *in* Wallace, R.E., ed., The San Andreas Fault system, California: U.S. Geological Survey Professional Paper 1515, p. 61–80.

Kelson, K.I., Simpson, G.D., Lettis, W.R., and Haraden, C.C., 1996, Holocene slip rate and recurrence of the northern Calaveras fault at Leyden Creek, eastern San Francisco Bay region: Journal of Geophysical Research, v. 101, p. 5961–5975.

King, M.S., 1966, Wave velocities in rocks as a function of changes in overburden pressure and pore fluid saturants: Geophysics, v. 31, p. 50.

Kissling, E., Husen, S., and Haslinger, F., 2001, Model Parameterization in seismic tomography, a choice of consequence for the solution quality: Physics of the Earth and Planetary Interior, v. 123, p. 89–101.

Lawson, A.C., 1908, The California Earthquake of April 18, 1906, Report of the State Earthquake Investigation Commission: Carnegie Institution of Washington, n. 87, 451 p.

Li, Y. -G., and Leary, P.C., 1990, Fault zone trapped seismic waves: Bulletin of the Seismological Society of America, v. 80, p. 1245–1271.

Mayer-Rosa, D., 1973, Travel time anomalies and distribution of earthquakes along the Calaveras fault zone, California: Bulletin of the Seismological Society of America, v. 72, p. 901–910.

Mooney, W. D., and Luetgert, J. H., 1982, A seismic refraction study of the Santa Clara Valley and southern Santa Cruz Mountains, west central California: Bulletin of the Seismological Society of America, v. 72, p. 901–909.

Mooney, W. D., and Ginzburg, A., 1986, Seismic measurements of the internal properties of fault zones: Pure and Applied Geophysics, v. 124, p. 141–157.

Niemi, T.M., and Hall, N.T., 1992, Late Holocene slip rate and recurrence of great earthquakes on the San Andreas fault in northern California: Geology, v. 20, p. 195–198.

Nur, A., and Simmons, G., 1969, The effect of saturation on velocity in low porosity rocks: Earth and Planetary Science Letters, v. 7, p. 183–193.

Nur, A., 1982, Stanford rock physics progress report, January 1982: Stanford Junior University, Stanford, California, v. 13, 121p.

Page, B.M., 1981, The southern Coast Ranges, *in* Ernst, W.G., ed., The geotectonic development of California (Rubey Volume 1): Englewood Cliffs, New Jersey, Prentice-Hall, p. 329–417.

Pampeyan, E.H., 1994, Geologic map of the Montara Mountain and San Mateo 7-1/2' quadrangle, San Mateo County, California: U.S. Geological Survey Miscellaneous Investigation Series Map I-2390, Scale 1:24,000.

Parsons, T., and Zoback, M.L., 1997, Three-dimensional upper crustal velocity structure beneath San Francisco Peninsula, California: Journal of Geophysical Research, v. 102, p. 5473–5490.

Prentice, C.S., 1999, San Andreas fault: The 1906 earthquake and subsequent evolution of ideas, *in* Moores, E.M., Sloan, D., and Stout, D.L., eds., Classic Cordilleran Concepts: A View from California: Boulder, Colorado, Geological Society of America Special Paper 338, p. 79–85.

Prentice, C.S., and Moreno, X., 2007, Paleoseismic site on the Peninsula San Andreas fault near Crystal Springs Reservoir: Preliminary results: Seismological Research Letters, v. 78, p. 315.

Prentice, C.S., Sickler, R.R., Hecker, S., Schwartz, D.P., and Brown, J., 2008, Preliminary results from a new paleoseismic site on the San Andreas fault near Crystal Springs Reservoir, San Francisco Peninsula, California: Seismological Research Letters, v. 79, p. 360.

Proctor, R.J., 1968, Geology of the Desert Hot Springs—Upper Coachella Valley area, California: California Division of Mines and Geology Special Report, v. 94, 50 p.

Rymer, M.J., Hickman, S.H., and Stoffer, P.W., 2006, A field guide to the central, creeping section of the San Andreas fault and the San Andreas Fault Observatory at Depth, *in* Prentice, C.S., Scotchmoor, J.G., Moores, E.M., and Kiland, J.P., eds., 1906 San Francisco Earthquake Centennial Field Guides: Fieldtrips associated with the 100th Anniversary conference, 18–23 April 2006, San Francisco, California: Geological Society of America Field Guide 7., p. 237–272, doi: 10.1130/2006.1906SF(16).

Savage, J.C., Svarc, J.L., and Prescott, W.H., 1999, Geodetic estimates of fault slip rates in the San Francisco Bay area: Journal of Geophysical Research, v. 104, p. 4995–5002.

Schussler, H., 1906, The water supply of San Francisco, California, before, during, and after the earthquake of April 18, 1906 and the subsequent conflagration. New York: Martin B. Brown Press, 103 p.

Sibson, R.H., 2003, Thickness of the seismic slip zone: Bulletin of the Seismological Society of America, v. 93, p. 1169–1178.

Sleep, N.H., and Fujita, K., 1997, Principles of Geophysics: Massachusetts, Blackwell Science, 586 p.

Spudich, P., and Angstman, B., 1980, Lateral variations in velocity and Q structure in the region of the 1979 Coyote Lake, California, earthquake: Earthquake Notes, v. 50, p. 64.

Steeples, D.W., and Miller, R.D., 1990, Seismic reflection methods applied to engineering, environmental, and groundwater problems, *in* Ward, S., ed., Geotechnical and Environmental Geophysics, v. 1: Society of Exploration Geophysicists, p. 1–30.

Thomsen, L., 1990, Poisson was not a geophysicist!: The Leading Edge, v. 9, p. 27–29, doi:10.1190/1.1439706.

Thurber, C. H., 1983, Earthquake locations and three-dimensional crustal structure in the Coyote Lake area, central California: Journal of Geophysical Research, v. 88, p. 8226–8236.

Tolman, C.F., 1937, Ground water: New York, McGraw-Hill, 593 p.

Toppozada, T.R., and Borchardt, G., 1998, Re-evaluation of the 1836 "Hayward Fault" and the 1838 San Andreas Fault Earthquakes: Bulletin of the Seismological Society of America, v. 88, p. 140–159.

Wallace, R.E., 1990 General Features, *in* Wallace, R.E., ed., The San Andreas Fault system, California: U.S. Geological Survey Professional Paper 1515, p. 3–13.

Wallace, R.E., and Morris, H.T., 1986, Characteristics of faults and shear zones in deep mines: Pure and Applied Geophysics, v. 124, p. 107–125.

Wang, C. Y., Lin, W., Wu, F. T., 1978, Constitution of the San Andreas Fault zone at depth: Geophysical Research Letters, v. 5, p. 741–744.

Wang, Z., 2001, Y2K Tutorial. Fundamentals of seismic rock physics: Geophysics, v. 66, p. 398–412.

Wesnousky, S.G., 1986, Earthquakes, Quaternary Faults, and Seismic Hazard in California: Journal of Geophysical Research, v. 91, p.12587–12631.

Wilson, J.E., Chester, J.S., and Chester, F.M., 2003, Microfracture analysis of fault growth and wear processes, Punchbowl Fault, San Andreas System, California: Journal of Structural Geology, v. 25, p. 1855–1873

Wood, H.O., and Neumann, F., 1931, Modified Mercalli Intensity Scale of 1931: Bulletin of the Seismological Society of America, v. 83, p. 277–283.

Working Group on California Earthquake Probabilities (WGCEP), 2003, Earthquake Probabilities in the San Francisco Bay Region: 2002-2031: U.S. Geological Survey Open-File Report 2003-214, 235 p.

2007 Working Group on California Earthquake Probabilities (WGCEP), 2008, The Uniform California Earthquake Rupture Forecast, Version 2 (UCERF 2): U.S. Geological Survey Open-File Report 2007-1437, CGS Special Report 203, SCEC Contribution #1138, Version 1.0, 104 p.

Wu, F.T., 1978, Mineralogy and physical nature of clay gouge: Pure and Applied Geophysics, v. 116, p. 655–689.

Zachariasen, J.A., Prentice, C.S., Kozaci, O., Sickler, R.R., Baldwin, J.N., Sanquini, A., and Knudsen, K.L., 2010, Paleoseismic study on the Peninsula segment of the San Andreas Fault south of Crystal Springs Reservoir, San Mateo County, California, American Geophysical Union, Fall Meeting 2010, abstract #S21C-2048.

Zachariasen, J.A., Baldwin, J.N., Kozaci, O., and Prentice, C., 2011, Paleoseismic investigations of Holocene earthquake recurrence on the Peninsula segment of the

San Andreas fault, Woodside, CA: Final Technical Report for USGS National Earthquake Hazard Reduction Program Award Number G09AP00048, 32 p.

Zhu, F., Gibson Jr., R.L., Watkins, J.S., and Yuh, S.H., 2000, Distinguishing water saturation changes form porosity or clay content changes using multicomponent seismic data: Gulf Coast Association of Geological Societies Transactions, v. L, p. 249–258.

Table 1: Relevant Previous Paleoseismic Studies on the Peninsula Segment of the San Andreas Fault

Study	Location	Slip Rate	Other Notable Findings
Hall et al., 1999	Filoli Estate, Woodside, CA	17 ± 4 mm/yr	Evidence for 1906 event. Proposed evidence for 1838 event based on channel deposit (dated at 330 ± 200 years B.P.), but refuted by Zacharaisen et al., 2010.
Prentice and Moreno, 2007; Prentice et al., 2008	10 km NW of study site, at N end of Lower Crystal Springs Reservoir		Identified 1906 rupture and one previous event; age constraints suggest older event occurred between AD 890–1260
Prentice et al., 2008	Same location as above.		Evidence for 1906 rupture and no previous event in their 3-m exposure
Baldwin et al., 2006; Baldwin and Prentice, 2008	16 km SE of study site, Portola Valley, CA		Evidence for at least three, possibly four pre-1906 events in 1000 years; no evidence for an 1838 event
Zachariasen et a., 2011	At the study site		Evidence for 1906 and previous event 600–1000 years ago; no evidence for 1838 event

Table 2: Summary of Wood and Neumann's Modified Mercalli Intensity Scale (1931)

MMI	Description
I. Instrumental	Generally not felt except by very few under favorable conditions.
II. Weak	Felt only by a few people that are sensitive, especially on upper floors of buildings. Delicately suspended objects may swing mildly.
III. Slight	Noticeably felt by people indoors, especially on upper levels. May not be recognized as earthquake. Vibration is similar to passing truck.
IV. Moderate	Felt by many indoors and outdoors by few. Dishes, windows, and doors rattle alarmingly. No damage.
V. Rather Strong	Felt inside by most everyone. Dishes and windows may break and vibrations resemble light train. Possible slight damage to buildings.
VI. Strong	Felt by everyone. Books and dishes fall off shelves. Windows are broken. Damage slight to moderate in poorly designed buildings.
VII. Very Strong	Difficult to stand. Damage light in well-designed buildings and considerable damage in poorly built structures.
VIII. Destructive	Damage slight in well-designed structures but considerable in normal buildings with a possible partial collapse. Damage great in poor structures.
IX. Violent	Considerable damage in well-designed structures and substantial buildings may partially collapse. Buildings shifted off foundations.
X. Intense	Well-built structures severely damaged to destroyed. Large landslides. Rails bent.
XI. Extreme	Few, is any, (masonry) structures will remain standing. Cracks and deformations of the ground and bridges destroyed.
XII. Catastrophic	Total destruction. Lines of sight and level distorted and objects are thrown into the air. Ground moves in waves or ripples and the landscape is altered or leveled by several meters.

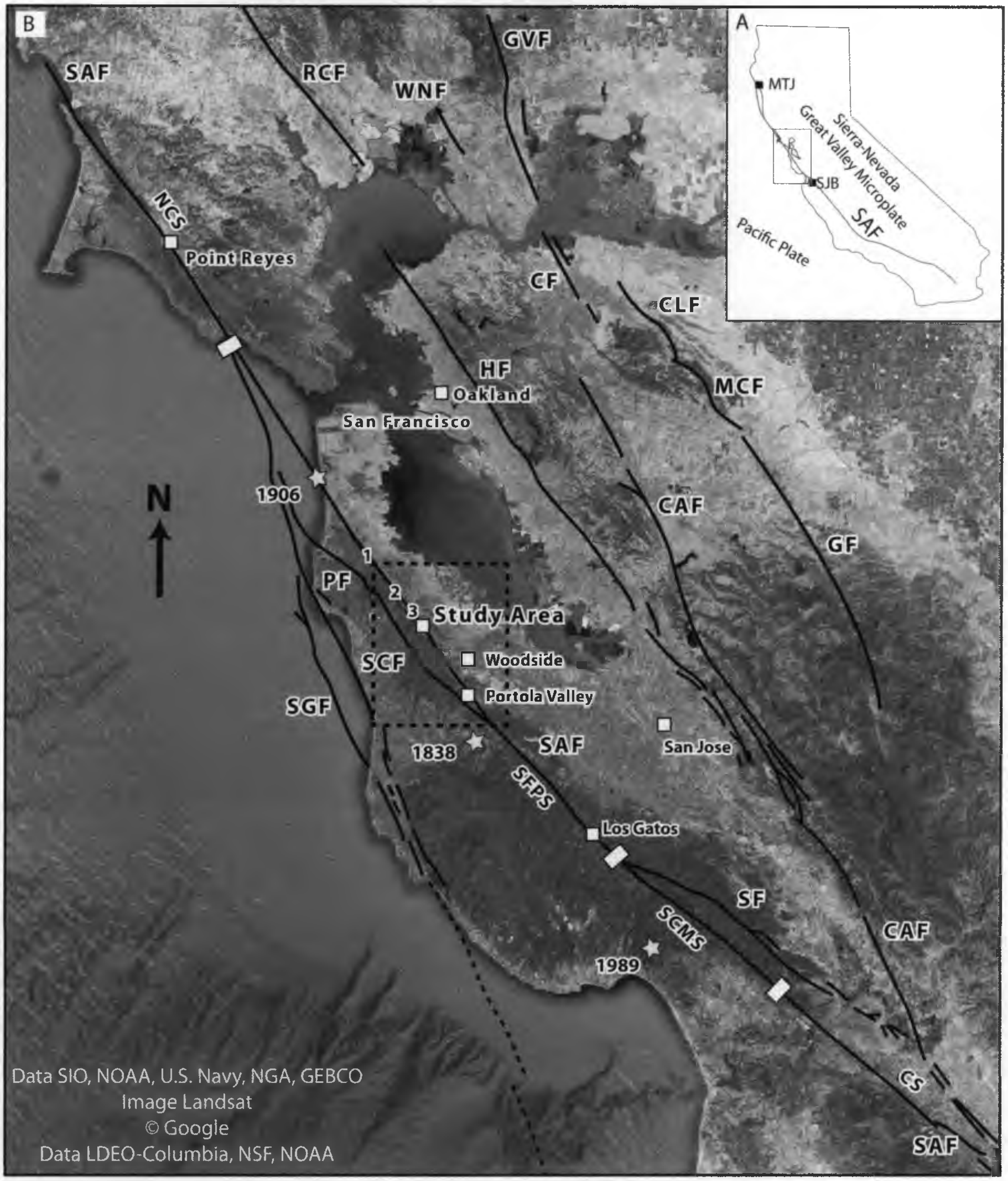

Figure 1: (A) Outline of California showing the 1,300 km extent of the San Andreas Fault (SAF), boundary between the Pacific plate and the Sierra Nevada-Great Valley microplate, MTJ = Mendocino Triple Junction; SJB = San Juan Bautista. (B) Annotated Google (2013) satellite image of the San Francisco Bay Area showing the SAF and other

major faults: CAF = Calaveras fault; CF = Concord fault; GF = Greenville fault; GVF = Green Valley fault; HF = Hayward fault; MCF = Marsh Creek fault; PF = Pilarcitos fault; RCF = Rogers Creek fault; WNF = West Napa fault; SCF = Seal Cove fault; SGF = San Gregorio fault; and SF = Sargent fault; Study area = Filoli Center. Open rectangles indicate segment boundaries of northern California SAF (NCS = North Coast; SFPS = San Francisco Peninsula; SCMS = Santa Cruz Mountains), and boundary between northern and central California (CS) sections. Yellow stars = historical earthquakes (1906 = M 7.9; 1989 = M 6.9; 1838 ~6.8-7.4). Numbers are locations: 1 = San Andreas Lake; 2 = Lower Crystal Springs Reservoir; 3 = Upper Crystal Springs Reservoir. Dashed box = location of Figure 3.

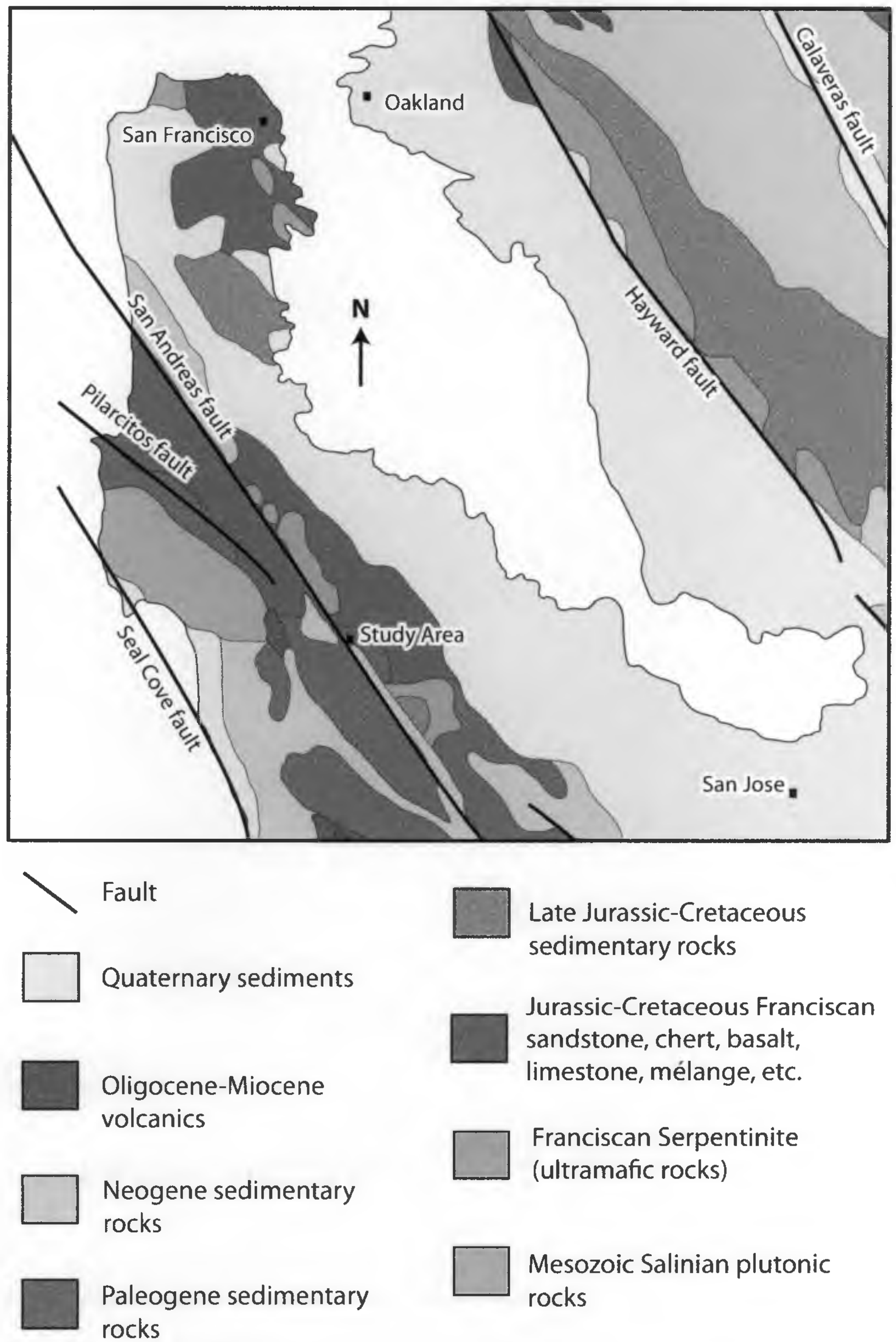

Figure 2: Generalized geologic map of the San Francisco Peninsula and East Bay regions showing surficial deposits, principal faults and cities. Adapted from Stoffer, 2002.

Figure 3: Annotated Google Earth (2013) satellite image showing location of study area and previous paleoseismic sites.

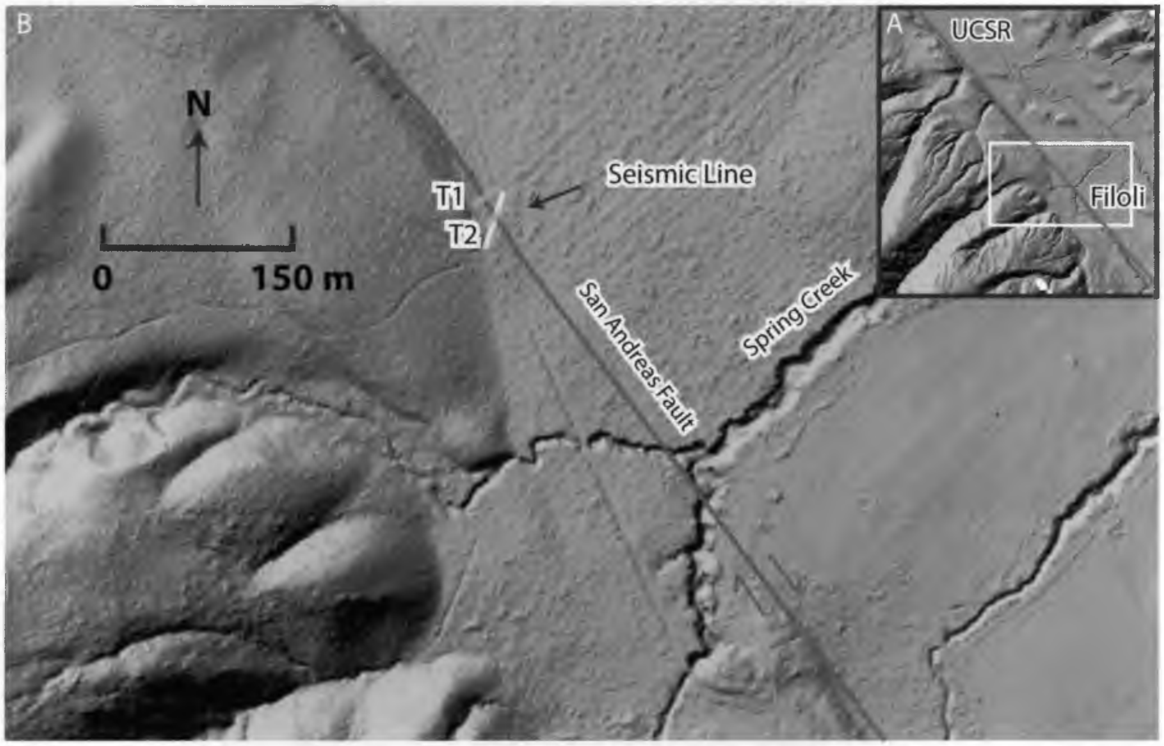

Figure 4: (A) LiDAR from National Science Foundation Geoearthscope showing location of study area (B) relative to Upper Crystal Springs Reservoir (UCSR) and the Filoli Center (Filoli). (B) LiDAR of the study area showing the seismic line location and the locations for two trenches (T1 and T2) opened by Zachariasen et al. (2011). The main location of the San Andreas Fault is shown in red in (A) and (B) from USGS/CGS fault database.

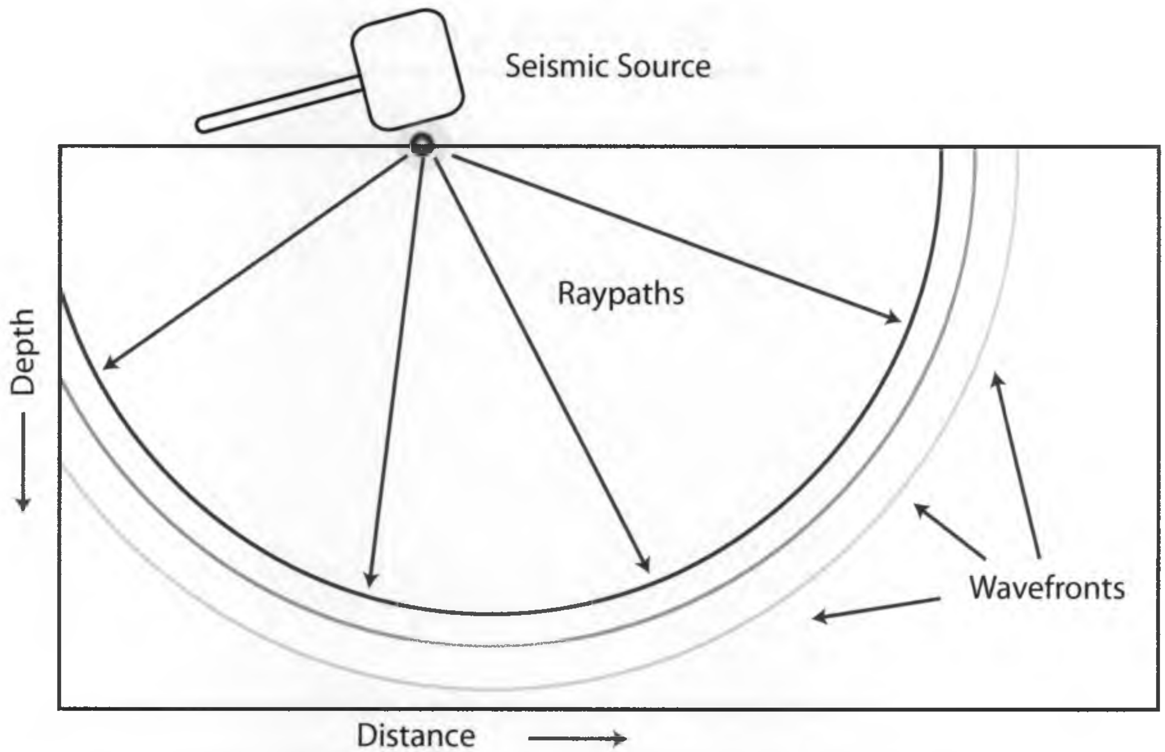

Figure 5: Schematic diagram of path of seismic energy/waves in the subsurface. Hemispherical wavefronts connect positions of seismic energy traveling in unison with the same amplitude. Adapted from Burger et al., 2006.

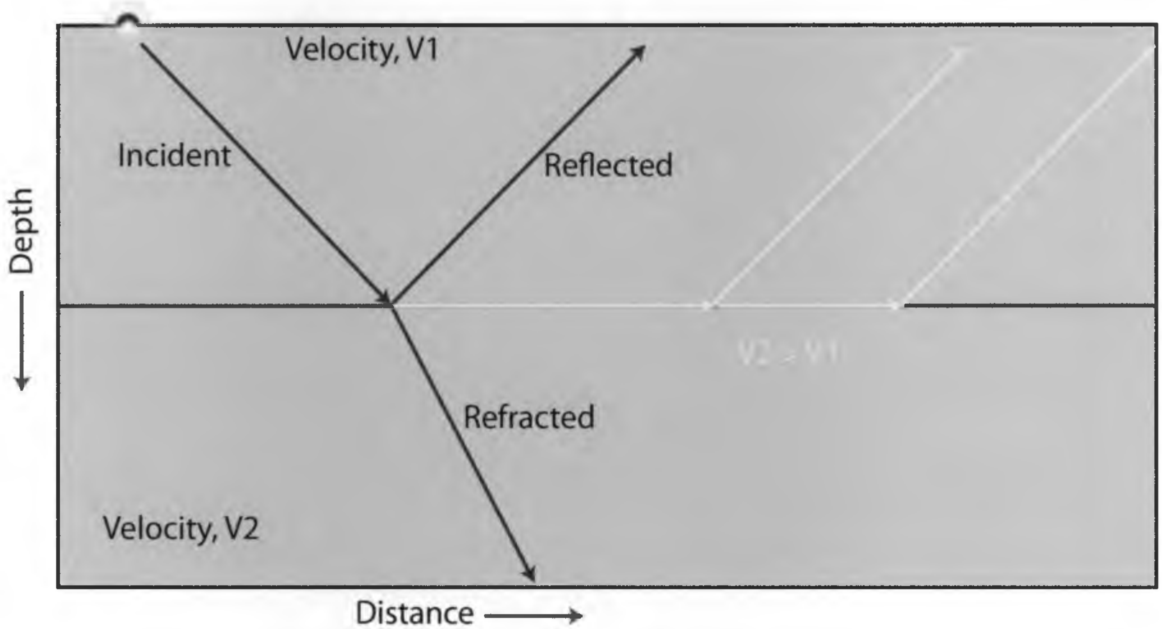

Figure 6: Diagram showing cases of reflected and refracted waves. When an incident wave (the initial incoming wave) reaches an interface between two materials with acoustical impedance contrasts, some of the energy is reflected back into the first material and some is refracted (transmitted) into the second material. Seismic waves are refracted where velocity increases with depth and this wave propagates along the interface with the lower medium's higher velocity. This happens because as the wavefront moves away from the source (to the right in this diagram), it acts as a moving source of waves that propagate back into the upper material with the lower material's velocity, V2. Adapted from Burger et al., 2006.

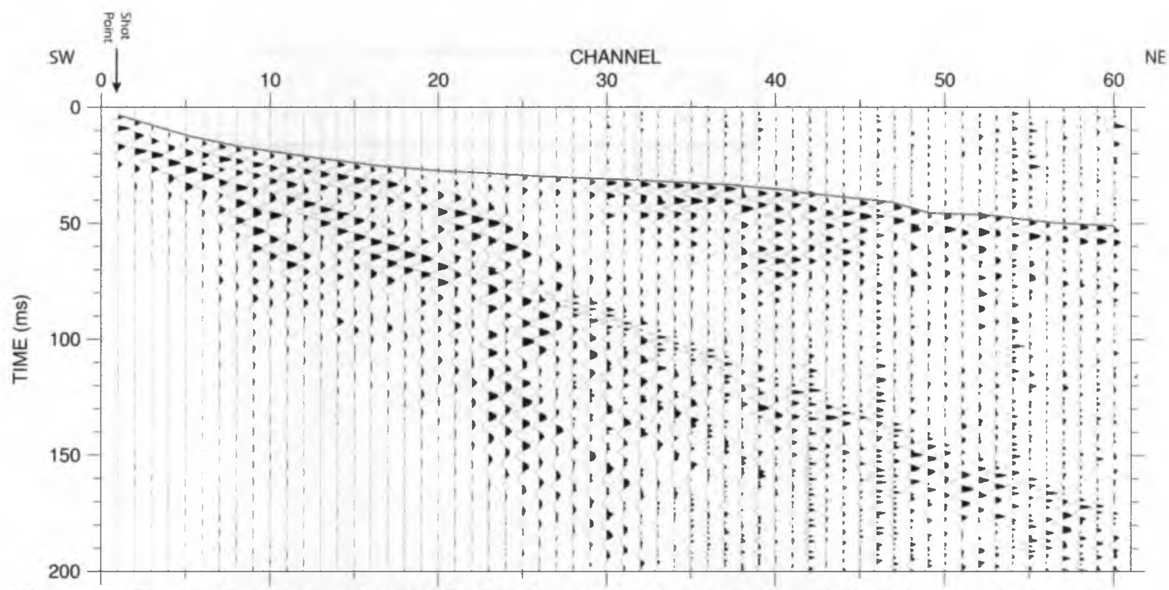

Figure 7: Example shot gather with the shot point (source) located at the southwestern end of the profile at geophone #1 (also shotpoint #1). The vertical axis is time in ms and the horizontal axis shows the channel number of the recording geophones, which is equivalent to distance along the profile in meters. Each vertical "wiggle" is a trace. The red line shows the first arrival times that were picked for seismic refraction analysis, which are always refracted rays.

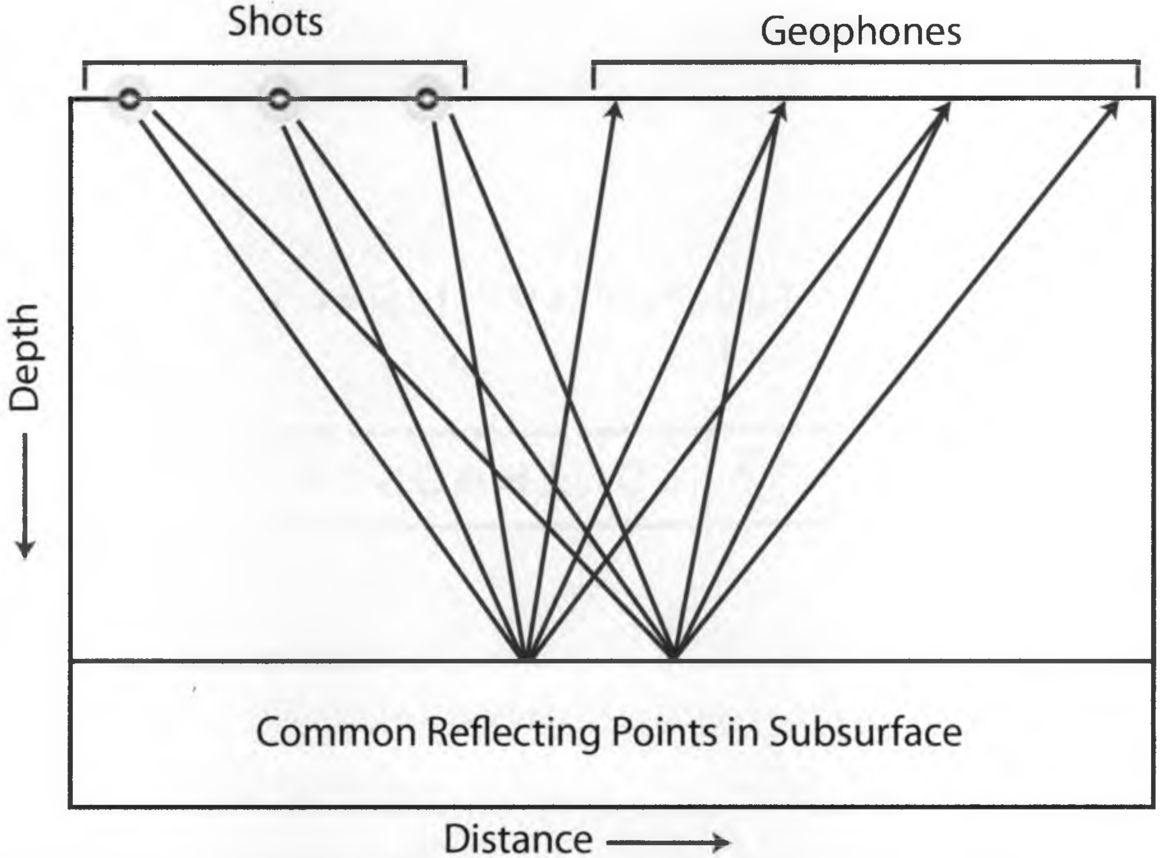

Figure 8: Diagram showing the raypaths for reflections from two common reflecting points in the subsurface. The technique is optimal for use in seismic surveying because many reflections from the same subsurface point are sampled at different shot-geophone pairs. Because of the seismic survey acquisition layout, geophones remained fixed in their positions throughout each shot, providing a dataset containing many common depth points (CDPs) to stack during processing. Adapted from Dobrin and Savit, 1988.

Figure 9: Field site showing seismic line marked by blue flags, which indicate the locations of the sources and geophones.

Figure 10: Photo showing method for P-wave generation. A hammer is used to trigger data recording when hit vertically on a steel plate (denoted by yellow star) placed every 1 m.

Figure 11: Photo showing method for S-wave generation. An aluminum box with cleats (to add shear to the surface) is placed every 1 m, while a hammer is used to trigger data collection. The block is struck on both ends multiple times (signified by yellow arrows) to force the block to move perpendicular relative to the seismic profile.

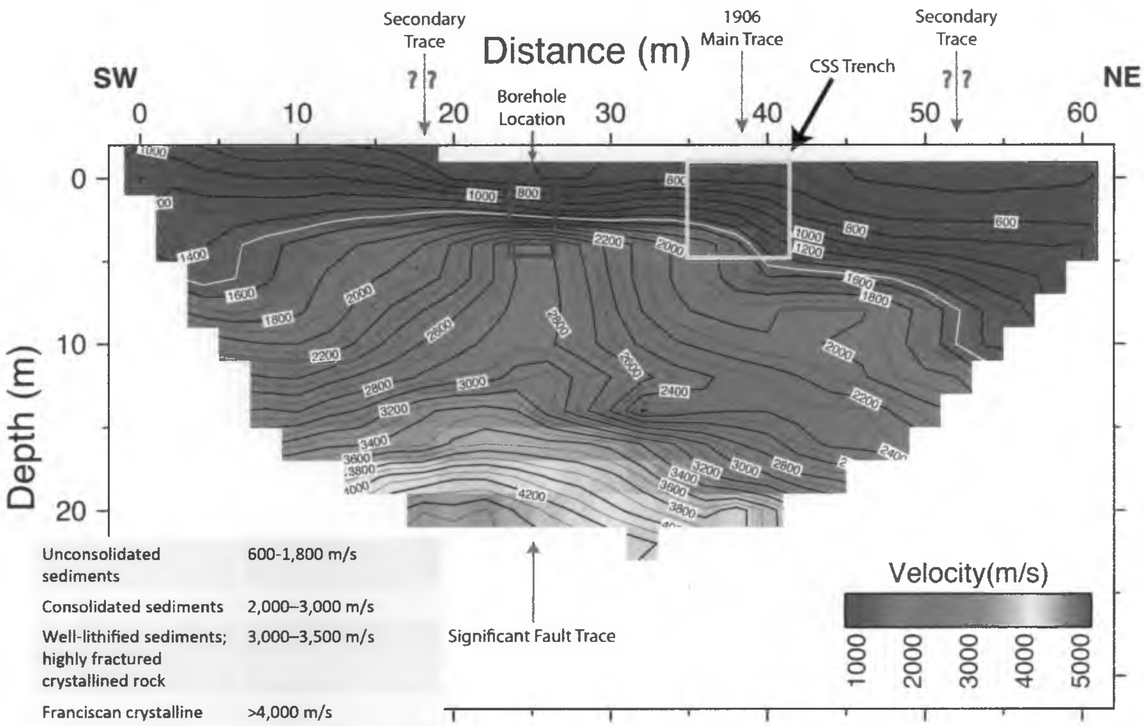

Unconsolidated sediments	600-1,800 m/s
Consolidated sediments	2,000–3,000 m/s
Well-lithified sediments; highly fractured crystallined rock	3,000–3,500 m/s
Franciscan crystalline	>4,000 m/s

Figure 12: P-wave refraction tomography velocity model for SAF profile (see Figure 4). Red arrows show location of the main fault trace at distance meter 38, and locations of possible secondary traces at distance meters 18 and 52. The 1,500 m/s contour (white line) correlates with the depth to the top of groundwater. A significant fault trace within the P-wave, high-velocity zone is located at distance meter 25. The red and yellow boxes show the locations for the hand-augered borehole and the trench by Zacharaisen et al. (2011), respectively. The bottom left table shows typically P-wave velocities for sediments and rocks.

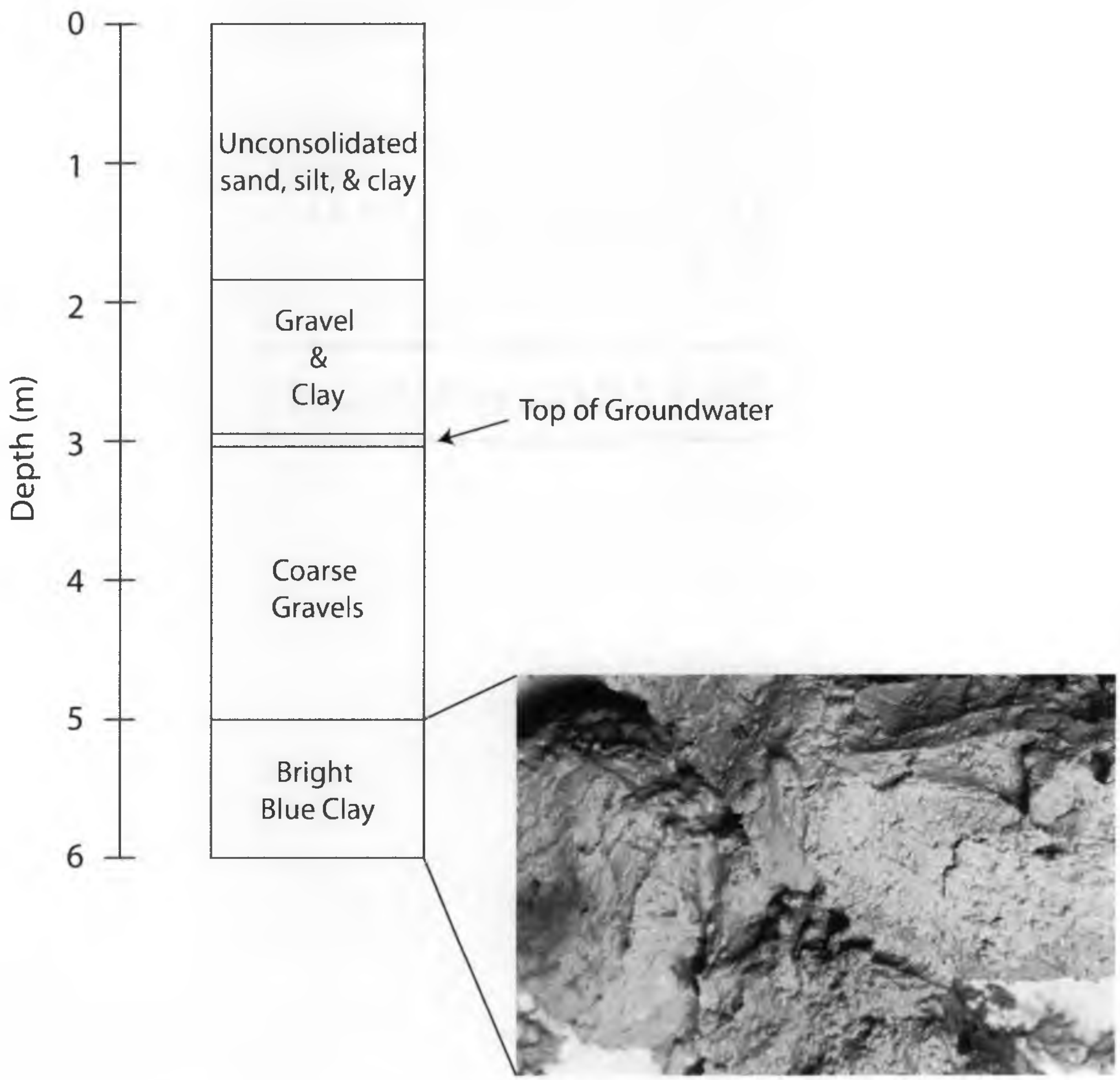

Figure 13: Stratigraphic sequence from borehole located at distance meter 25 of the seismic profile. Photo is blue clay at bottom of the borehole.

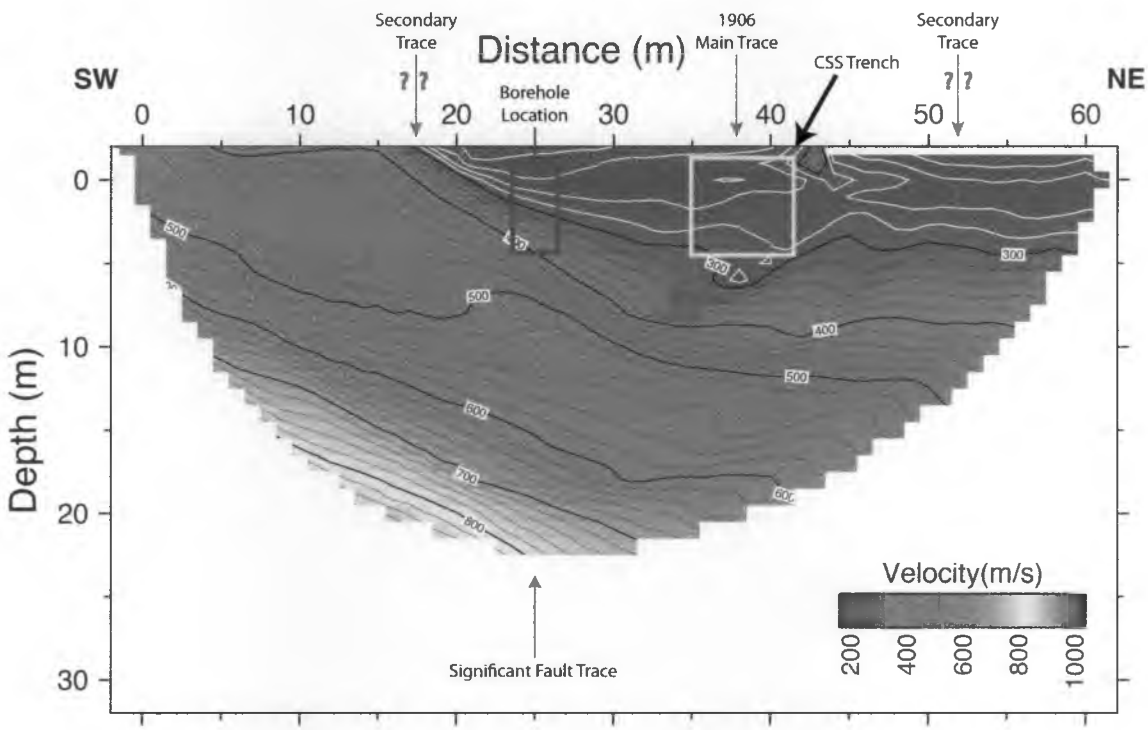

Figure 14: S-wave refraction tomography velocity model for the SAF profile (see Figure 4). The red arrows indicate locations for the main 1906 fault trace at distance meter 38, and possible secondary fault traces at distance meters 18 and 52. A significant fault trace within the P-wave, high-velocity zone is located at distance meter 25. The red and yellow boxes show the locations for the hand-augered borehole and the trench by Zacharaisen et al. (2011), respectively.

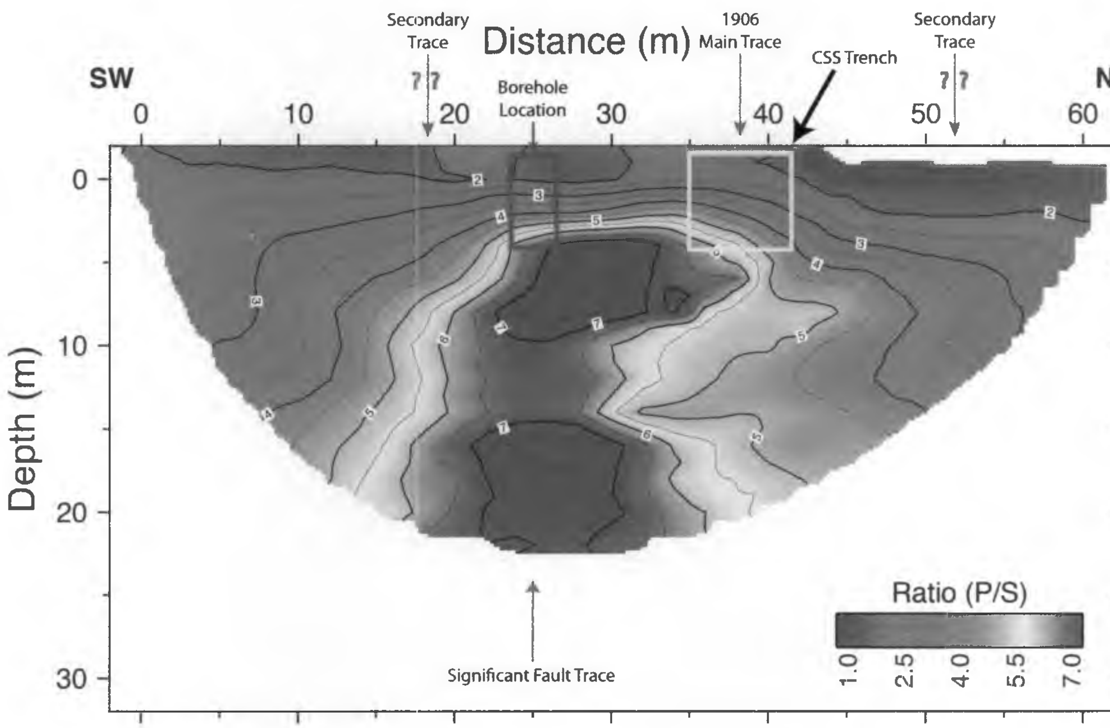

Figure 15: Vp/Vs ratio image along the SAF profile (see Figure 4). The relatively high Vp/Vs ratios extend from the near-surface main trace of the fault to the maximum imaging depth. The red arrows indicate locations for the main 1906 fault trace at distance meter 38, and possible secondary fault traces at distance meters 18 and 52. A significant fault trace within the P-wave, high-velocity zone that correlates with the highest Vp/Vs ratios is located at distance meter 25. The red and yellow boxes show the locations for the hand-augered borehole and the trench by Zacharaisen et al. (2011), respectively.

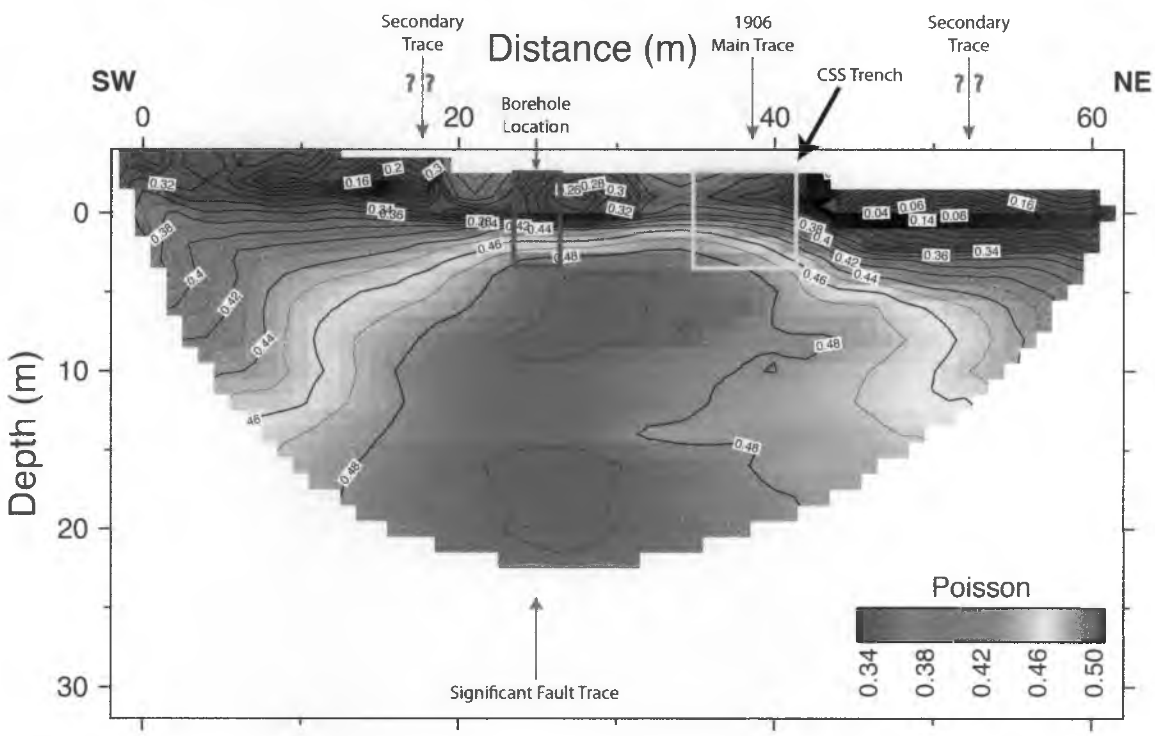

Figure 16. Poisson's ratio (PR) image along the SAF profile (see Figure 4). The red arrows indicate locations for the main 1906 fault trace at distance meter 38, and possible secondary fault traces at distance meters 18 and 52. A significant fault trace within the P-wave, high-velocity zone that correlates with the highest Vp/Vs ratios is located at distance meter 25. The red and yellow boxes show the locations for the hand-augered borehole and the trench by Zacharaisen et al. (2011), respectively.

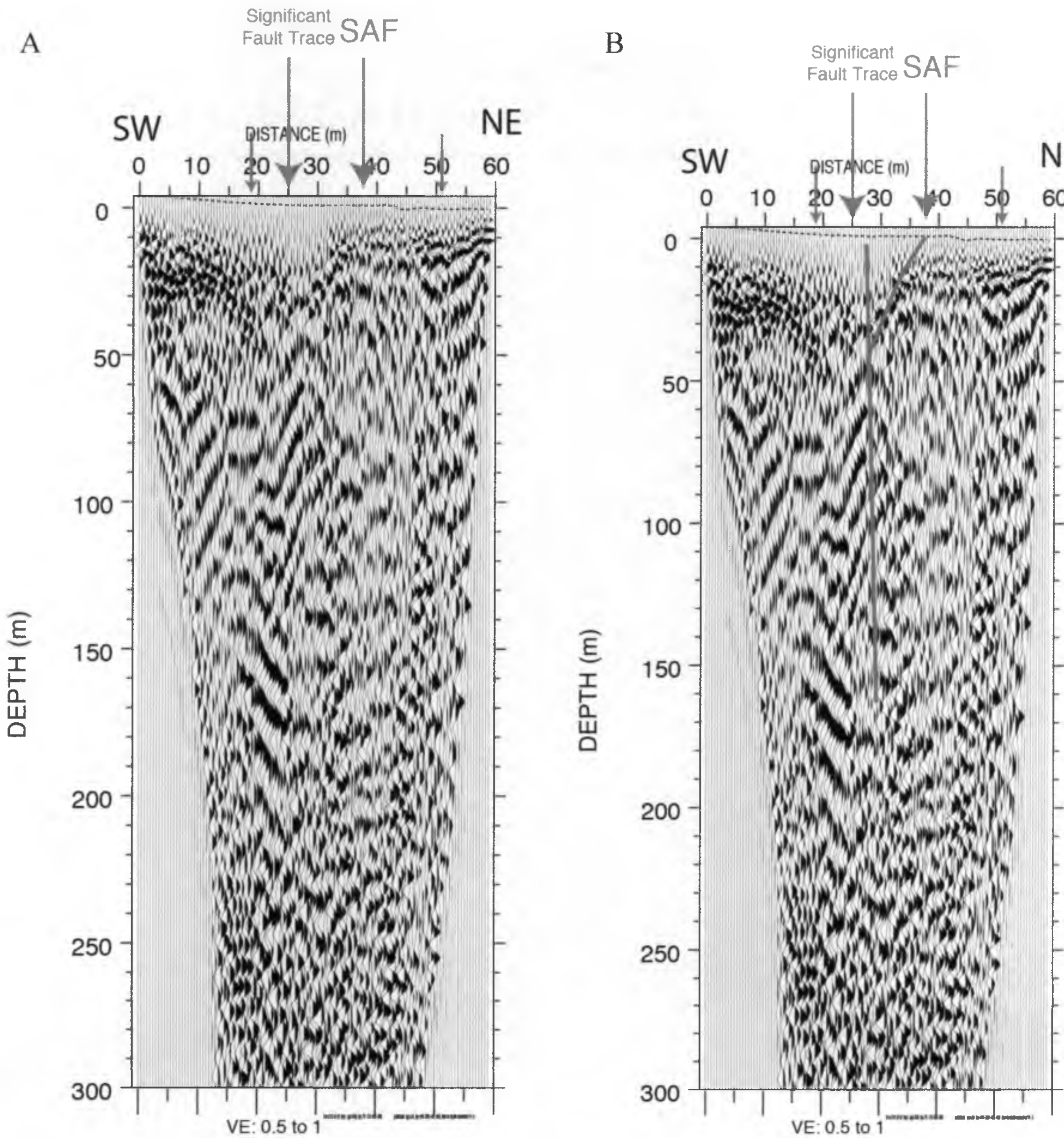

Figure 17: (A) Stacked, unmigrated reflection image and (B) same stacked reflection image with interpretations for fault traces at depth along the SAF seismic profile (see Figure 4). The red arrows indicate locations for the main 1906 fault trace at distance meter 38, the significant fault trace at distance meter 25, and possible secondary fault traces at distance meters 18 and 52.

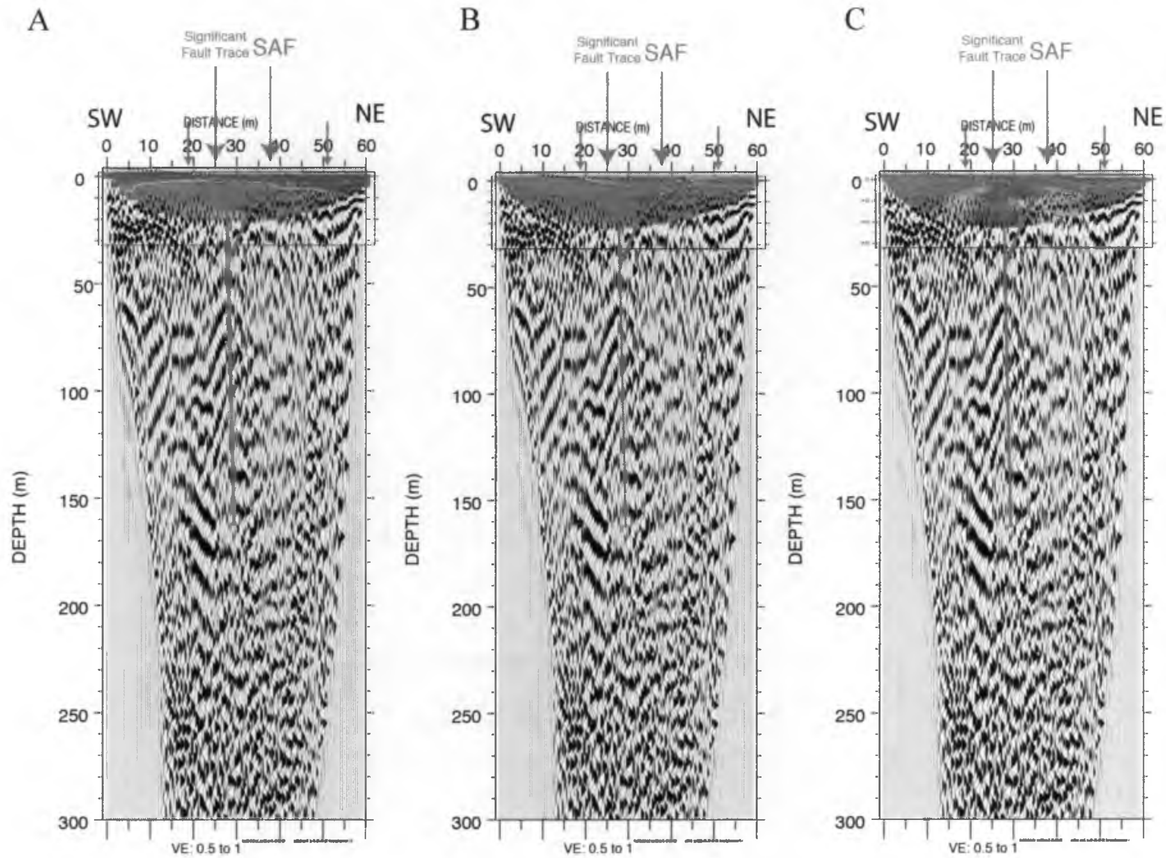

Figure 18: Stacked, unmigrated reflection image with interpretations for fault traces at depth along the SAF seismic profile (see Figure 4) with (A) superimposed Vp model, (B) superimposed Vs model, and (C) superimposed Vp/Vs ratios model. The red arrows indicate locations for the main 1906 fault trace at distance meter 38, the significant fault trace at distance meter 25, and possible secondary fault traces at distance meters 18 and 52.